AGU PUBLICATIONS

JGR

Journal of Geophysical Research: Oceans

RESEARCH ARTICLE

10.1002/2017JC012792

Key Points:
- Pacific equatorial wind stress and the dipole mode index drive steric variability in the Tropical Asian Seas
- The first principal component of the wind stress explains a large fraction of the mass variability
- Omitting the Tropical Asian Seas in global budgets decreases the sea level trend by 0.3 mm/yr

Supporting Information:
- Supporting Information S1

Correspondence to:
M. Kleinherenbrink,
m.kleinherenbrink@tudelft.nl

Citation:
Kleinherenbrink, M., R. Riva, T. Frederikse, M. Merrifield, and Y. Wada (2017), Trends and interannual variability of mass and steric sea level in the Tropical Asian Seas, *J. Geophys. Res. Oceans*, *122*, 6254–6276, doi:10.1002/2017JC012792.

Received 10 FEB 2017
Accepted 11 JUL 2017
Accepted article online 13 JUL 2017
Published online 9 AUG 2017

Trends and interannual variability of mass and steric sea level in the Tropical Asian Seas

Marcel Kleinherenbrink[1], Riccardo Riva[1], Thomas Frederikse[1], Mark Merrifield[2], and Yoshihide Wada[3,4,5,6]

[1]Department of Geoscience and Remote Sensing, Delft University of Technology, Netherlands, [2]Department of Oceanography, University of Hawaii, Honolulu, Hawaii, USA, [3]NASA Goddard Institute for Space Studies, New York City, New York, USA, [4]Center for Climate Systems Research, Columbia University, New York City, New York, USA, [5]Department of Physical Geography, Utrecht University, Utrecht, Netherlands, [6]International Institute for Applied Systems Analysis, Laxenburg, Austria

Abstract The mass and steric components of sea level changes have been separated in the Tropical Asian Seas (TAS) using a statistically optimal combination of Jason satellite altimetry, GRACE satellite gravimetry, and ocean reanalyses. Using observational uncertainties, statistically optimally weighted time series for both components have been obtained in four regions within the TAS over the period January 2005 to December 2012. The mass and steric sea level variability is regressed with the first two principal components (PC1&2) of Pacific equatorial wind stress and the Dipole Mode Index (DMI). Sea level in the South China Sea is not affected by any of the indices. Steric variability in the TAS is largest in the deep Banda and Celebes seas and is affected by both PCs and the DMI. Mass variability is largest on the continental shelves, which is primarily controlled by PC1. We argue that a water flux from the Western Tropical Pacific Ocean is the cause for mass variability in the TAS. The steric trends are about 2 mm yr^{-1} larger than the mass trends in the TAS. A significant part of the mass trend can be explained by the aforementioned indices and the nodal cycle. Trends obtained from fingerprints of mass redistribution are statistically equal to mass trends after subtracting the nodal cycle and the indices. Ultimately, the effect of omitting the TAS in global sea level budgets is estimated to be 0.3 mm yr^{-1}.

1. Introduction

Sea level trends in the Tropical Asian Seas (TAS) over the altimetry era (1993–present) are among the highest in the world [*Cazenave and Le Cozannet*, 2013]. The region is especially vulnerable to sea level rise due to the many low-lying densely populated areas [*Strassburg et al*., 2015]. Additionally, groundwater depletion in large cities as Manilla, Bangkok, and Jakarta [*Phien-Wej et al*., 2006; *Rodolfo and Siringan*, 2006; *Chaussard et al*., 2013; *Raucoules et al*., 2013] causes subsidence and enhances societal and economic risks. Furthermore, the TAS form an interesting area in both sea level and oceanographic studies, because they serve as a passage for dynamical interactions between the Pacific and Indian oceans [*Wijffels and Meyers*, 2004].

Many studies considered sea level variability in areas surrounding the TAS, mostly focussing on the Western Tropical Pacific Ocean (WTPO). The large sea level trends during the altimetry area in the WTPO are attributed to strengthening of the trade winds since the 1990s [*Merrifield*, 2011; *Merrifield and Maltrud*, 2011; *Zhang and Church*, 2012; *England et al*., 2014]. Interannual and decadal variability in trade winds are related to the El Niño Southern Oscillation (ENSO) and the Pacific Decadal Oscillation (PDO), who cause steric fluctuations in the WTPO region. Furthermore, several studies indicated that the ENSO and PDO are also driving the sea level in the Leeuwin Current at Fremantle [*Feng et al*., 2004; *Lee and McPhaden*, 2008; *Merrifield et al*., 2012], which requires waves to propagate through the southern parts of the TAS. The trade winds associated with the PDO are expected to weaken over the coming years [*Zhang and Church*, 2012; *England et al*., 2014], which will lead to lower sea level trends in the WTPO and the Leeuwin current, but also in the TAS [*Strassburg et al*., 2015].

Even though many studies described the relation between sea level, heat content, ENSO, and PDO in the TAS area and surroundings, the contributions of other sources are often neglected. *McGregor et al*. [2012a]

suggests that an additional mass component is required to be able to capture the full sea level rise signal. For the South China Sea and east of the Philippines, this is confirmed by *Rietbroek et al*. [2016], who performed an inversion on altimetry and Gravity Recovery And Climate Experiment (GRACE) data to obtain trends in sea level driven by global mass redistribution and steric changes. They estimated that at least 25% of the total sea level rise between 2002 and 2014 in the SCS and east of the Philippines, respectively, 7.6 and 14.7 mm yr^{-1}, is due to mass changes.

So far only in the South China Sea have mass and steric components have been separated using GRACE and ocean reanalyses or in situ measurements of temperature and salinity [*Feng et al*., 2012]. The limited number of studies is mainly due to the absence of Argo temperature and salinity measurements and a commonly applied cut off of GRACE data in the first 300 km from the coast to avoid hydrological signal leakage. Not considering the individual mass and steric components in the TAS no only limits the understanding of sea level variability in the region itself, but it also affects studies on larger scales. *Von Schuckmann et al*. [2014] showed that the TAS region is responsible for nonclosure of the sea level budget in the tropics, caused by the significantly larger sea level trends in the TAS, and that the omission of the TAS leads to a trend discrepancy of 0.5 ± 0.2 mm yr^{-1} in global sea level budgets over the January 2005 to December 2010 period.

In this study, we use for the first time altimetry, optimally filtered GRACE solutions and temperature and salinity fields from ocean reanalysis products to separate steric from mass contributions to sea level between January 2005 and December 2012. We derive dedicated variance-covariance matrices for altimetry, use full variance-covariance matrices stemming from GRACE data processing and use the spread of steric sea levels from six ocean reanalyses to obtain a statistically optimal separation between mass and steric sea level. This allows for a correction of global and large-scale regional sea level budgets to the steric and mass components in the TAS, which have been omitted in previous studies [*Willis et al*., 2008; *Leuliette and Willis*, 2011; *Von Schuckmann et al*., 2014]. Additionally, we investigate the dynamical mass response in shallow regions to the larger steric response in the deeper ocean and couple both the steric and mass components to the ENSO and the Dipole Mode Index (DMI). The ENSO contribution is investigated in further detail by considering the first two Principal Components (PC) of the Equatorial wind stress as is done in *McGregor et al*. [2012b] and *Widlansky et al*. [2014]. Finally, we quantify how much the mass trend is affected by the tidal nodal cycle and by global mass redistribution.

2. Study Area

To study the TAS in more detail, we separate it into four regions as shown in Figure 1. Region A, the South China Sea is characterized by deep bathymetry in the center and relatively large shallow areas near the Chinese and Vietnamese coasts. Several Argo floats are present in region A, but not enough to allow for an accurate interpolation.

Region B, referred to as Thailand-Java, is characterized by very shallow bathymetry, typically less than 100 m. The steric sea level is poorly constrained due to the absence of any Argo float measurements and the presence of only a few shipboard measurements of temperature and salinity. GRACE observations are largely affected by the 2004 Andaman-Sumatra Earthquake in this region and therefore, we exclude all observations before 2005. However, as will be discussed in section 3.2, the postseismic relaxation of the solid Earth still affects observations. Furthermore, as well as in region A, the neighboring Mekong basin might introduce a substantial hydrological leakage, which is also further discussed in section 3.2.

Region C, denoted as Banda-Celebes, is very deep, but the area is divided by many islands into several small basins, with their own regime. As a result the correlation scales of sea level variability in this area are shorter than in an open basin, like region A.

Region D is slightly deeper than region B, with maximum depths of 200–300 m. Together with region C, it is subjected to the throughflow from the Pacific to the Indian Ocean. In the southwest, region D is connected to the Leeuwin Current, where sea levels strongly depend on Pacific Ocean indices, like the PDO and the ENSO as mentioned in the introduction. This region will be referred to as Timor-Arafura.

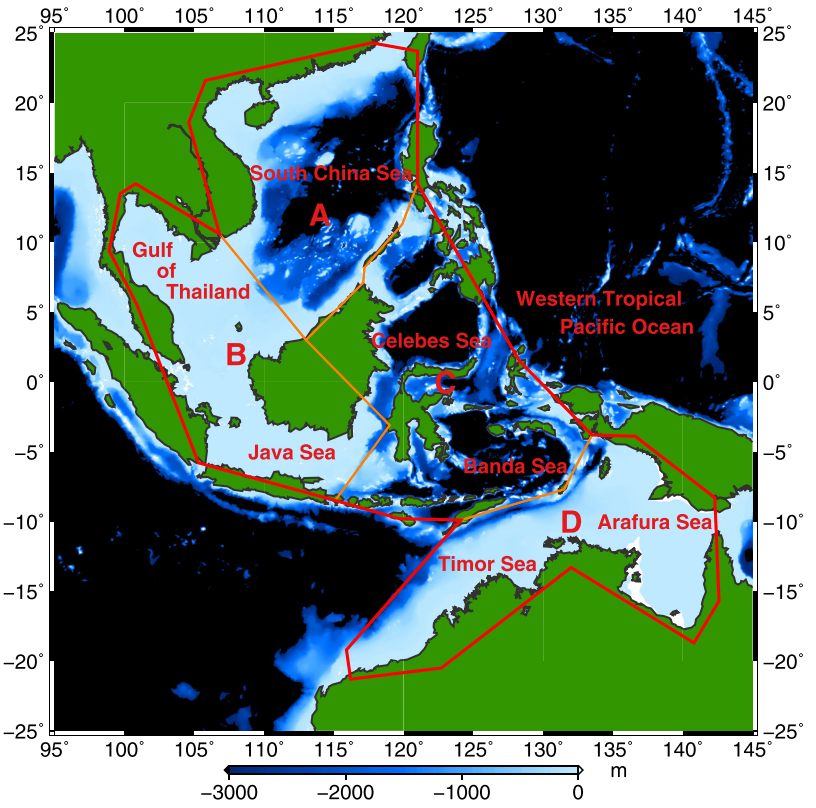

Figure 1. Bathymetry and topography in and around the TAS. Visible are four averaging regions. In tables, we refer to the regions as A, B, C, and D for brevity.

3 Data and Methods

To obtain a consistent separation of the mean mass $\bar{h}_{mass}$ and steric sea level $\bar{h}_{steric}$, it is required that the sea level budget equation [*Leuliette and Miller*, 2009]

$$\bar{h}_{total} = \bar{h}_{mass} + \bar{h}_{steric} \tag{1}$$

is closed within error bars. While the observation of mean total sea level $\bar{h}_{total}$ in the TAS can be done with altimetry using standard techniques, estimating the mass and steric components is less trivial. The mass component is obtained from GRACE gravity fields, which need to be corrected for contamination by leakage of hydrological signals and gravitational effects of the Sumatra-Andaman earthquake. The absence of Argo floats in the TAS causes difficulties in estimating the steric component and therefore we rely on ocean reanalyses. This introduces additional problems, since most of the reanalysis products are volume conserving and have a resolution that cannot capture the detailed structure of the TAA. This section will explain how the different observations and models are used in order to obtain a statistically optimal separation between the mass and steric components.

To explain the behavior of the steric sea level and mass components, we regress indices and principal components (PC) and use mass redistribution fingerprints. This section also describes how the PC of the equatorial wind stress are obtained and briefly introduces the sea level equation, which is used to obtain the fingerprints.

3.1. Altimetry Mean Sea Level

The Mean Sea Level Anomaly (MSLA) is estimated from along-track Jason-1&2 altimetric sea level measurements, obtained from the Radar Altimetry Database System (RADS) [*Scharroo et al.*, 2012], averaged over the regions indicated in Figure 1. Range corrections used to acquire sea level estimates are the same as in *Kleinherenbrink et al.* [2016] and are given in Table 1. Additionally, we apply a latitude dependent intermission bias [*Ablain et al.*, 2015; *Kleinherenbrink et al.*, 2016]. The Sea Level Anomaly (SLA) is then obtained by

Table 1. List of Geophysical Correction Applied in This Study

Ionosphere	Smoothed Dual-Frequency
Wet troposphere	Radiometer
Dry troposphere	ECMWF
Ocean tide	GOT4.10
Loading tide	GOT4.10
Pole tide	Wahr
Solid Earth tide	Cartwright
Sea state bias	Tran2012
Dynamic atmosphere	MOG2D

subtracting the DTU13 mean sea surface [*Andersen et al.*, 2015] from the corrected sea level measurements. Surface area weighting of the SLAs is done by dividing the ocean area A_l in a latitude band l of 1° by the number of measurements N_l, such that

$$\omega_i = \frac{A_l}{N_l} \tag{2}$$

are the nonnormalized weights for measurement i inside a particular latitude band l. The weights are normalized, which results in:

$$w_i = \frac{\omega_i}{\sum \omega_i}. \tag{3}$$

The latitude-dependent covariance functions of *Le Traon et al.* [2001] are not suitable to obtain error bars for the MSLAs in the TAS due to islands, currents, and depth variations. For every averaging region, a dedicated covariance function is therefore estimated. First, we compute the dissimilarity $\gamma_{i,j}$ between all the measurements over a 10 day repeat period:

$$\gamma_{i,j} = \frac{(h_i - h_j)^2}{2}, \tag{4}$$

where h_i and h_j are two SLAs within the considered region in a 10 day repeat orbit relative to a background field, which is a second-order polynomial fit through all the measurements in the region during the Jason-1 period. A variogram $\hat{\gamma}_n$ is created by binning and averaging dissimilarities into 20 km range bins n, to have enough measurements per bin to reduce the noise, which are then averaged over all 10 day repeat periods of Jason-1. Using the variance $\hat{\sigma}_h^2$ of the background removed SLAs, the experimental covariance between measurements is computed as:

$$\hat{c}_n = \hat{\sigma}_h^2 - \hat{\gamma}_n. \tag{5}$$

We considered Gaussian, spherical and exponential covariance functions, and found that the exponential one fits the experimental covariances best. Using the weight vector $\hat{w}$, the distance between the measurements and the fitted covariance functions, the standard error $\sigma_{\bar{h}}$ for mean sea level time series is computed, such that:

$$\sigma_{\bar{h}} = \hat{w}^T C_{total} \hat{w}, \tag{6}$$

where C_{total} is the variance-covariance matrix of the measurements computed from the exponential fit. In addition we add an error to the time series, related to the drift in the altimeter system [*Mitchum*, 1998, 2000], which is given as:

$$\epsilon_{drift} = \alpha(t - t_0), \tag{7}$$

with t the time in years, t_0 the time of the middle epoch of the time series, and $\alpha = 0.4$ mm yr^{-1}.

3.2. GRACE Ocean Mass

To minimize leakage and reduce striping effects, an anisotropic Wiener filter [*Klees et al.*, 2008] is applied to the GRACE gravity fields. The ITSG-Grace2016 spherical harmonic solutions are selected, because they give the best overall performance in combination with the Wiener filter in previous work about the North Atlantic [*Kleinherenbrink et al.*, 2016]. Let x be a vector of monthly spherical harmonic ITSG coefficients, then the resulting filtered coefficients are given as:

$$x_f = (D_x^{-1} + N_x)^{-1} N_x x, \tag{8}$$

which rely on the signal variance-covariance matrix D_x and the normal matrix N_x of the solution. The corresponding noise variance-covariance matrix $C_{x,f}$ is computed as:

$$C_{x,f} = (D_x^{-1} + N_x)^{-1}. \quad (9)$$

The derivation of the Wiener filter is provided in *Klees et al*. [2008] and the derivation of the variance-covariance matrix is found in *Kleinherenbrink et al*. [2016]. Note that the monthly mean of background dealiasing products (GAD) has to be added to get the full signal. The mean of GAD product over the ocean is removed, to make GRACE compatible with altimetry corrected for the inverse-barometer. Averaging over a region is performed by weighting with the cosine of the latitude as described by *Kleinherenbrink et al*. [2016].

The mass variability on the continental shelves of the TAS is large with amplitudes reaching 10 cm. The load causes the ocean floor to move several millimeters, which cannot be neglected. Altimetry measures absolute sea level and GRACE, the mass component relative to the ocean floor, therefore we will add the ocean floor motion to the GRACE-derived mass time series. To compute the ocean floor motion, the GAC instead of the GAD product is added to the GRACE products, which includes atmospheric pressure over land [*Fenoglio-Marc et al*., 2012]. Consecutively, we compute ocean floor motion from monthly GRACE gravity fields in spherical harmonics as [*Wahr et al*., 1998; *Fenoglio-Marc et al*., 2012]:

$$Y_{vlm}(l,m) = Y_{ewl}(l,m)\frac{3\rho_w}{\rho_e}\frac{h_l}{2l+1}, \quad (10)$$

where the $Y_{ewl}(l,m)$ and $Y_{vlm}(l,m)$ the spherical harmonic coefficients at degree/order (l, m) in equivalent water height and vertical land motion, respectively. The constants ρ_w and ρ_e denote the densities of water and the Earth, while h_l is the Love number that relates the body tide to the static equilibrium tide. The resulting vertical land motion affects the trends up to 0.4 mm yr^{-1} and has an annual cycle with an amplitude up to 3 mm.

3.2.1. Hydrological Signal Leakage

From the PCRaster GLOBal Water Balance (PCR-GLOBWB), we obtain monthly averaged Terrestrial Water Storage (TWS), including surface water [*Wada et al*., 2011]. Groundwater depletion is not considered. Although cities, like Jakarta, extract large quantities of groundwater, the limited resolution TWS model does not include this effect. We expect that ground water depletion does not have a significant influence on the trends, because of the difference in scale between the averaging regions and the groundwater depletion zones. Using the TWS, one can obtain an estimate for the hydrological signal leakage of GRACE gravity fields into the surrounding ocean in terms of equivalent water level. We do this by reducing the resolution of TWS grids to that of the ITSG-Grace2016 and by applying the corresponding filter parameters. Based on the PCRGLOBWB data, the TAA area typically has TWS variability ranging from several centimeters up to decimeters, which is confirmed by a comparison with GRACE in the Mekong basin by *Tangdamrongsub et al*. [2016].

The ITSG-Grace2016 monthly gravity fields are provided as departure from the GOCO05s model, which contains a static field, a trend, and an annual cycle [*Klinger et al*., 2016]. To be consistent with the (post-)processing of ITSG-Grace2016 as done in *Kleinherenbrink et al*. [2016], we first isolate the mean, the trend, and the annual signal independently for each grid point, which we refer to as the background signal. Then the background signal, excluding the mean, and the residual signal are both converted to spherical harmonics and truncated at degree-and-order 90. The degree 0 and 1 terms for the background and residual signal are set to zero and the background signal is converted back to a grid. The same filtering is applied to the spherical harmonics of the residual signal as in equation (8) and the signal is converted back to a spatial grid. The resulting hydrological leakage has a negligible effect on the time series, the trend and the annual cycle in case of the ITSG-Grace2016 gravity fields. However, this might be different for other GRACE products, such as CSR, which do not compute the gravity field solutions with respect to a background trend and annual cycle.

3.2.2. Sumatra-Andaman Earthquake

The gravity field in the Thailand-Java region is strongly affected by the 2004 Sumatra-Andaman earthquake. Even though our time series starts in 2005, postseismic deformation affects the obtained mass and geoid trends [*Broerse et al*., 2015]. We also will remove the effect of the earthquake before the statistical separation discussed in section 3.4. A regression is made of a logarithmic relaxation function (representing postseismic effects), a trend, annual, and semiannual cycles, PC1&2 of the wind stress and Dipole Mode Index (DMI) to

Table 2. Reanalyses Used in This Study

Reanalysis	Resolution (°)	References
GODAS	1 × 0.33	*Behringer and Xue* [2004]
GFDL CM2.1[a]	1 × 1	*Zhang et al.* [2007]
ECCO-JPL	1 × 1	*Forget et al.* [2015]
GECCO2 R1	1 × 0.33	*Köhl* [2015]
ORAS4	1 × 1	*Balmaseda et al.* [2013]
ORAP5.0[a]	0.25 × 0.25	*Zuo et al.* [2015]
Glorys2V3[a]	0.25 × 0.25	*Ferry et al.* [2010]
SODA v3.3.1	0.5 × 0.5	*Carton and Giese* [2008]

[a]Tripolar grids.

reduce as much variability as possible in the time series of region B. Long-term ocean dynamics, as represented by the mentioned indices, might correlate with the relaxation function and therefore excluding them might lead to significantly different regression parameters [*Einarsson et al.*, 2010]. The computation of PC1&2 is explained in section 3.5. We will also remove the effect of the nodal cycle before the regression with the mass time series, of which the computation is given in section 3.7. The logarithmic relaxation function is given as [*Hetland and Hager*, 2006]:

$$u_{\ln,t} = A \cdot \ln\left(1 + \frac{t - t_{eq}}{\tau_{\ln}}\right), \tag{11}$$

where the magnitude A is the parameter to be estimated in the regression and t_{eq} the time of the Sumatra-Andaman earthquake. The relaxation time is $\tau_{\ln} = 5$ yr, which corresponds to the mean relaxation time found by *Broerse et al.* [2015]. The regression is repeated for the 95% confidence intervals of $\tau_{\ln} = 1.5$ and $\tau_{\ln} = 20.8$ yr (provided by *Broerse et al.* [2015]) to get an estimate of the spread. A time-dependent standard error is then estimated by subtracting both relaxation functions and dividing them by four. The error is referenced such that it is largest directly after the earthquake and decays to zero at the end of the time series. Eventually, the geoid and mass relaxation functions are subtracted from, respectively, the total sea level derived from altimetry and the mass component derived from GRACE.

3.3. Steric Sea Level

The steric sea level is inferred from reanalysis temperature and salinity fields using the TEOS-10 package [*Pawlocwicz et al.*, 2012], which requires profiles of absolute salinity S_A, conservative temperature Θ, and pressure P'. Using the gravitational constant g_0 and the atmospheric pressure P_0, the steric sea level is computed as [*IOC et al.*, 2010; *Kleinherenbrink et al.*, 2016]:

$$h_{rean} = -\frac{1}{g_0}\int_{P_0}^{P} \hat{\delta}(S_A(P'), \Theta(P'), P')dP', \tag{12}$$

with respect to a reference pressure P. The reanalysis products considered in this study are given in Table 2. The reference pressure is in all cases set to either the local maximum depth in the models or limited to 2000 dBar, since the limited resolution of some of the models reduces the number of grid cells to a few tens below the reference depth. Not all reanalyses provide conservative temperature, so a conversion from potential to conservative temperature is applied using the TEOS-10 software package. In addition we add a virtual temperature and salinity observation at 0.5 dBar depth, because the steric sea level is computed at the top pressure level, which varies between 0 and 10 dBar, so that the whole steric signal is captured [*Kleinherenbrink et al.*, 2016]. The virtual temperature and salinity observations have the same values as observations in the top layer of the reanalysis product.

As provided in the table, the resolution and the type of grid vary for the reanalyses. For the tripolar grids, steric sea levels are averaged onto a 0.5°×0.5° (Glorys and ORAP5) or a 1°×1° (GFDL) grid. Then, the steric sea levels are weighted with the cosine of their latitude to get a mean steric sea level for a region. Finally, the zero reference of the time series is set to the middle of the time series (approximately 2009) and then the RMS of the suite of reanalyses for each epoch (monthly) is used as an approximation of the error and the mean as the steric sea level for further analysis.

The ocean reanalyses all make specific choices on, among other factors, model specifications, horizontal and vertical resolution, and assimilated techniques. Therefore, over parts of the oceans that are not well-constrained by direct observations, the model spread provides an estimate of the uncertainty of the ocean state. Since some covarying bias may exist between similar models, such as the models from the ECMWF

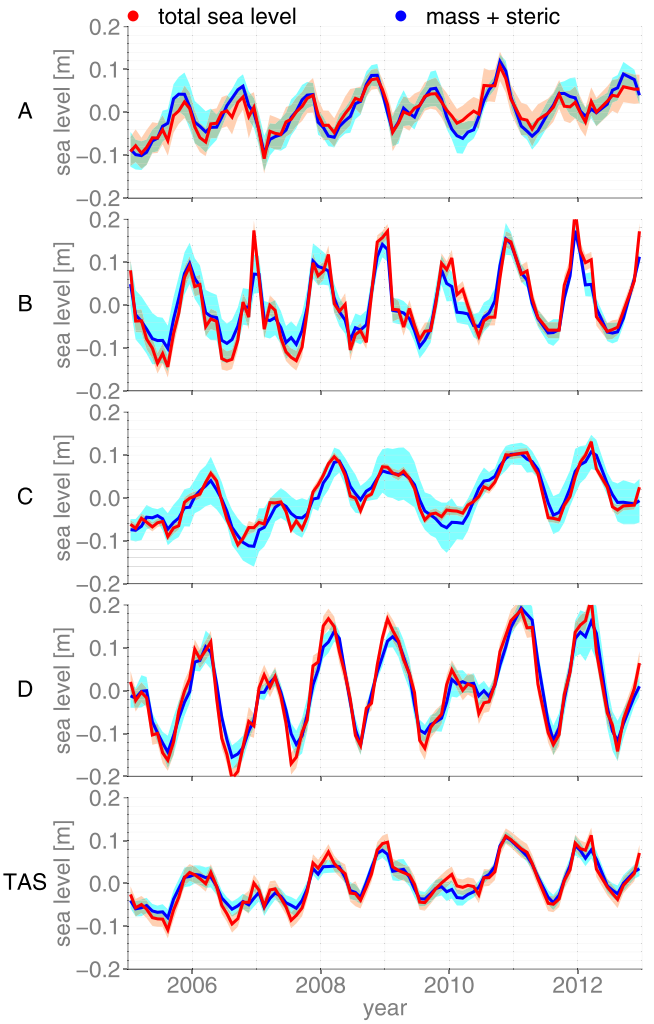

Figure 2. Sea level time series for the subregions and the total TAS. The South China Sea, Thailand-Java, Banda-Celebes, and Timor-Arafura regions are, respectively, indicated with A, B, C, and D. In blue GRACE mass + steric sea level from the reanalyses. In red altimetry-derived total sea level.

ocean reanalysis project (ORAS4 and ORAP5), and to enhance the estimate of the underlying uncertainty of the ocean state, we use a large set of ocean reanalysis products from different modelling groups, which include the new generation of eddy-permitting ocean reanalyses, but also reanalyses on coarser grids. Table 2 lists the reanalysis that are used.

To check the stability of the mean time series from the eight products, a test is performed by each time omitting one reanalysis product. In case of outliers, one of the time series averaged over seven products should deviated significantly from the one averaged over eight reanalysis products. Based on this test, we find that the results are stable and no outliers are present (supporting information, Figure S1). All reanalyses are constrained by sea surface temperature, satellite altimetry sea surface height, a few CTD and XBT observations and in the surrounding areas and the South China Sea by Argo float observations. Since their physics are also quite similar, it is not expected that the computed steric sea levels to deviate significantly.

To examine the relative contributions of temperature and salinity to steric sea level, we compared time series of the full steric sea level against the thermosteric sea level (supporting information Figure S2). For the time series of thermosteric sea level, the salinity is kept constant at 35 PSU. Salinity changes only have an effect on the trends in regions A and B. In terms of interannual variability and annual cycles, the steric sea level variability is primarily driven by thermosteric changes in all regions.

For a comparison between the interannual variability of steric sea level of the WTPO with the mass component in the TAS in section 4.2, the independent gridded temperature and salinity product of *Roemmich and Gilson* [2009] is used, so that a correlation will not be an artifact of one of the models. Besides being independent, we expect that the interpolated grid of *Roemmich and Gilson* [2009] performs better in the WTPO than the reanalyses, particularly in terms of steric sea level trends as shown in *Kleinherenbrink et al.* [2016] over the North Atlantic Ocean. The interpolated grid cannot properly be used inside the TAS, due to a lack of observations at depth, so there we have to rely on the physics of the reanalysis products. This product is created by statistical interpolation of Argo float temperature and salinity measurements onto monthly 3-D grids with a horizontal resolution of $1^\circ \times 1^\circ$.

3.4. Statistical Separation

As shown in Figure 2, the time series of summed steric and mass and total sea level for the whole TAA do not always resemble each other within error bars. After subtracting the seasonal cycle (shown in the supporting information, Figure S3), it becomes clear that both methods capture the interannual variability, however they

still depart on occasion and their trends do not statistically resemble. Due to the lack of in situ data, it is difficult to determine where the discrepancies originate from. We assume that our errors properly represent the uncertainties in the data sets. Statistically weighting will then give a more consistent division between the mass and steric components, such that they better match the three observations of mass, steric, and total sea level.

The vector y_t for time step t contains three observations: the monthly low-pass filtered altimetric mean sea level $\bar{h}_{alt,t}$, the mean steric sea level $\bar{h}_{rean,t}$ computed from the reanalyses, and the mean mass $\bar{h}_{grace,t}$ from GRACE, such that:

$$y_t = \begin{pmatrix} \bar{h}_{alt,t} \\ \bar{h}_{rean,t} \\ \bar{h}_{grace,t} \end{pmatrix}, \quad Q_{yy,t} = \begin{pmatrix} \bar{\sigma}^2_{alt,t} & 0 & 0 \\ 0 & \bar{\sigma}^2_{rean,t} & 0 \\ 0 & 0 & \bar{\sigma}^2_{grace,t} \end{pmatrix}. \tag{13}$$

The variance-covariance matrix $Q_{yy,t}$ contains the standard errors of the observations: $\bar{\sigma}^2_{alt,t}$, $\bar{\sigma}^2_{rean,t}$, and $\bar{\sigma}^2_{grace,t}$, which are obtained as described in the first three methodology sections. Using the design matrix

$$A = \begin{pmatrix} 1 & 1 \\ 1 & 0 \\ 0 & 1 \end{pmatrix} \tag{14}$$

the statistically optimal mean steric sea level $\bar{h}_{steric,t}$ and mean mass $\bar{h}_{mass,t}$ are computed using least squares:

$$\begin{pmatrix} \bar{h}_{steric,t} \\ \bar{h}_{mass,t} \end{pmatrix} = (A^T Q^{-1}_{yy,t} A)^{-1} A^T Q^{-1}_{yy,t} y_t. \tag{15}$$

The corresponding variance-covariance matrix $Q_{\hat{x}\hat{x},t}$ is given by:

$$Q_{\hat{x}\hat{x},t} = (A^T Q^{-1}_{yy,t} A)^{-1}. \tag{16}$$

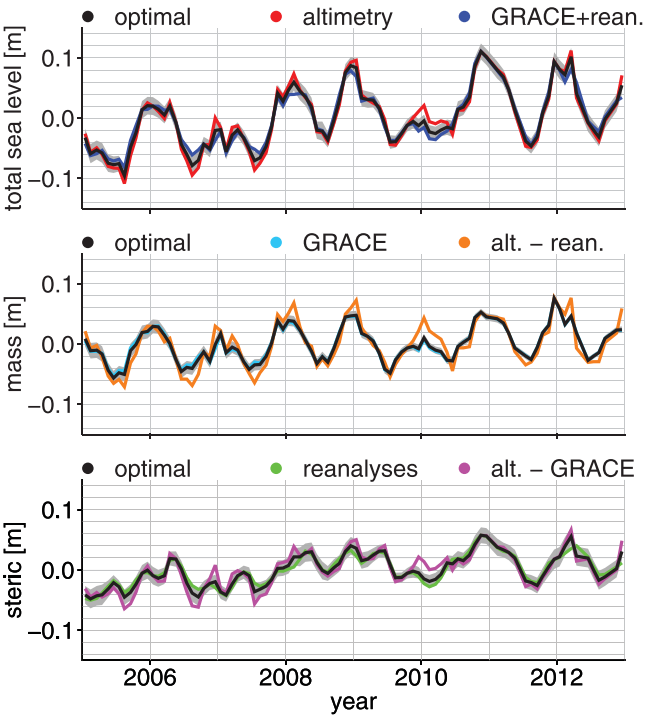

Figure 3. Time series of total and steric sea level and mass for the whole TAS region. (top) Total sea level from altimetry in red, from GRACE + reanalyses in blue, and the optimal solution in black. (middle) Mass from GRACE in light blue, from steric-corrected altimetry in orange, and the optimal solution in black. (bottom) Steric sea level from the reanalyses in green, from altimetry-GRACE in purple, and the optimal solution in black.

The resulting optimally weighted time series for the whole TAS region are given in Figure 3.

3.5. Wind Stress and the Dipole Mode Index

Widlansky et al. [2014] showed that sea level in the neighboring WTPO correlates with the first two principal components of the equatorial wind stress. The first PC represents eastward equatorial wind stress anomalies, which strongly correlates with the Niño 3.4 sea surface temperature anomalies [*McGregor et al.*, 2012b], while the second PC indicates the seasonal weakening and southward shift of anomalous winds during ENSO events.

To obtain the PCs the monthly ERA-Interim (version 2.0), 10 m wind speed is used between 10°S–10°N and 100°E–60°W as in *McGregor et al.* [2012b]. The wind stress (τ_x, τ_y) is estimated from the wind speed (u,v) using the relations [*Pugh and Woodworth*, 2014]:

$$\tau_x = \rho_{air} \frac{(0.8+0.065\sqrt{u^2+v^2})}{1000} u\sqrt{u^2+v^2}$$
$$\tau_y = \rho_{air} \frac{(0.8+0.065\sqrt{u^2+v^2})}{1000} v\sqrt{u^2+v^2}, \quad (17)$$

where ρ_{air} is the density of air. We create a 2-D-matrix with the wind stress time series in both directions for all $2^\circ \times 2^\circ$ grid cells over the whole data set (January 1979 to December 2015), so that we capture multiple La Nina and El Nino events. Before computing the covariance's the mean, the annual and semiannual signals are removed. The Empirical Orthogonal Functions (EOFs) are consecutively computed as the eigenvectors of the variance-covariance matrix of the remaining wind stress anomalies. PC1 and PC2 are the time series for the first two EOFs of the wind stress anomalies, accounting for 25% and 14% of the total anomaly variance (Figure 4).

PC1 peaks in El Niño periods and has troughs during La Niña (Figure 4), while PC2 peaks and troughs are slightly delayed with respect to PC1. The associated mode 1 spatial pattern (Figure 5), which shows the typical strong easterly wind stress anomaly associated the El Niño. This causes a positive temperature anomaly in the eastern equatorial Pacific and a weak negative temperature anomaly in the WTPO. *Meyers et al.* [2007] showed that during El Niño the sea surface temperature in regions B, C, and D (as given in Figure 1) of the TAS drops as well. During La Niña this pattern reverses, causing the thermocline to deepen in the WTPO, which leads to a positive sea level anomaly in the same area. In regions B, C, and D of the TAS, we find a positive sea surface temperature anomaly during La Niña events. In the following, significant correlations with PC1 represent variability that is in phase with ENSO and with PC2 variability associated with the seasonal weakening and southward shift of anomalous winds during ENSO events.

Additionally, we investigate the effects of interannual ocean dynamics from the Indian Ocean using the Dipole Mode Index (DMI). The DMI features peaks that at times align with ENSO events (e.g., 2006–2007, 2010–2011); however; overall the correlations between the DMI and PC1 and PC2 are low. When DMI is negative, a positive sea surface temperature anomaly occurs in the eastern Indian Ocean and in the TAS, with the opposite temperature anomaly for a positive DMI [*Meyers et al.*, 2007]. In case of a positive DMI and an El Niño state, the temperature anomalies, especially in the Banda-Celebes region (C) is strongly enhanced *Meyers et al.* [2007].

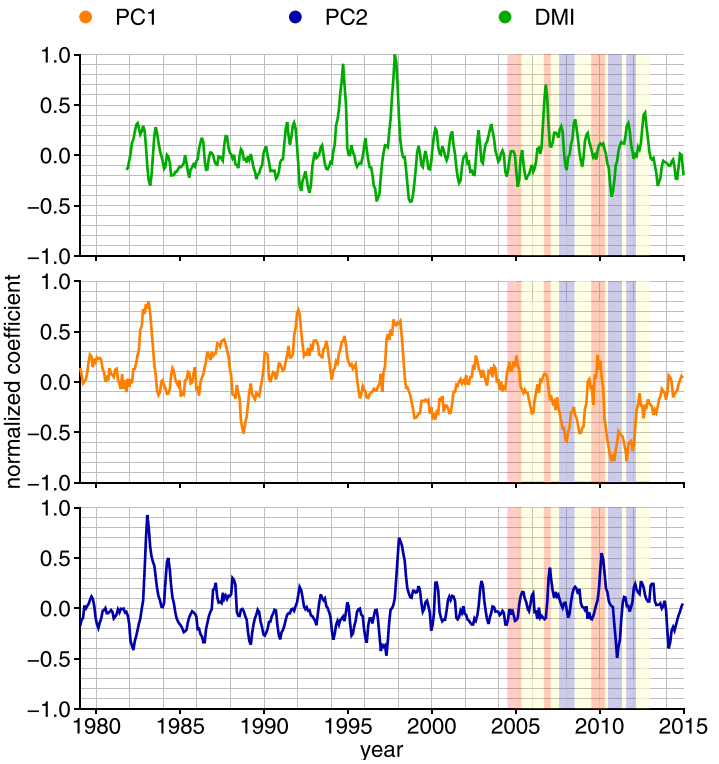

Figure 4. The first two PCs of the wind stress anomaly and the DMI. All low-pass filtered with a 3 month moving average filter to reduce high-frequency noise. The yellow-shaded area indicates the period January 2005 to December 2012 over which we have steric and mass time series. The red and blue shades indicate, respectively, El Niño and La Niña states as given by Climate Prediction Center of NOAA (http://www.cpc.ncep.noaa.gov/products/analysis_monitoring/ensostuff/ensoyears.shtml).

3.6. Present-Day Mass Redistribution

We compute the contribution to relative sea level associated with mass changes $\Delta L(\theta, \phi, t)$ due to Greenland, Antarctica, and glacier ice loss, land hydrology, and dam retention. These changes result into geoid height changes $\Delta G(\theta, \phi, t)$ and solid Earth height changes $\Delta R(\theta, \phi, t)$ and a global mass conservation term Λ, which are all related to each other, so that [*Tamisiea et al.*, 2010]

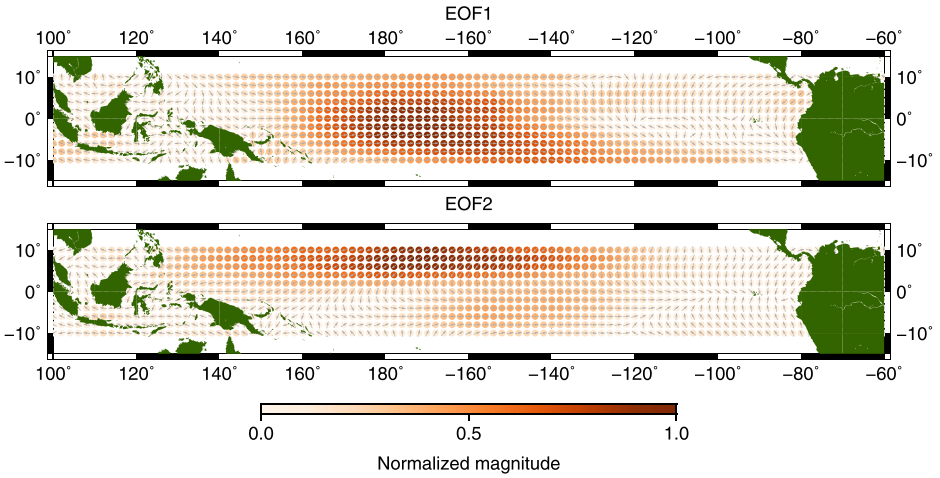

Figure 5. The first two EOFs corresponding to the PCs of the wind stress. The colors indicate the intensity of the wind stress and the vectors the direction.

$$\Delta S(\theta,\phi,t)=\Delta G(\theta,\phi,t)-\Delta R(\theta,\phi,t)+\Lambda, \tag{18}$$

where $\Delta S(\theta,\phi,t)$ is relative sea level change at longitude θ, latitude ϕ at time t. For the change in absolute sea level, we only require the change in geoid and the mass conservation term, which is estimated by solving the sea level equation including rotational feedback [*Farrell and Clark*, 1976; *Milne and Mitrovica*, 1996]. Details on the individual contributions are described in the supplement of *Frederikse et al.* [2016].

The resulting contributions to absolute sea level trends are computed for 2005.5–2012.5 (Figure 6). Note that the input loads are only given on yearly intervals. Only dam retention has a negative contribution to the sea level trend. Greenland is by far the largest contributor due to its substantial ice loss during the considered period and its remote location. The largest change in sea level is found far away from the source. The average sum of sea level trends explained by the mass transport obtained with the fingerprint procedure in the TAS is approximately 2.4 mm yr^{-1}. This is only a small fraction of the total sea level trend in the TAS. A comparison between the trends of fingerprints and the total sea level trends is shown in supporting information Figure S4.

3.7. Nodal Cycle

The effect of tidal nodal cycles on absolute sea level trend estimates has not been considered previously for the TAS and surrounding regions. The amplitude of the nodal cycle at the Equator is approximately 7 mm. Since the length of our time series is 8 years and the period of the nodal cycle is 18.61 years, we only capture part of the cycle, which can introduce mass trends at the millimeter-per-year level.

We evaluate the nodal cycle at the epochs of GRACE. According to *Proudman* [1960], the nodal cycle has a minimum at the equator at the reference time $t_0=2006.45$. The mean sea level $\bar{h}_{NC,t}$ in the considered region caused by the nodal cycle at time t is then given as:

$$\bar{h}_{NC,t}=\bar{\Omega}\cos\left(2\pi(t-t_0)\right), \tag{19}$$

where $\bar{\Omega}$ is the average amplitude over the considered region. We follow the equilibrium equations of *Proudman* [1960] to compute the amplitude Ω

$$\Omega=\alpha(1+k_2-h_2)(2\sin^2(\theta)-1), \tag{20}$$

in which θ is the latitude, α is the tidal magnitude, set to 8.8 mm following *Woodworth* [2011], and the tidal Love numbers are $k_2=0.36$ and $h_2=0.60$. Using the approach described in *Woodworth* [2011] and *Frederikse et al.* [2016], geoid changes resulting from the applied load are computed using the sea level equation from section 3.6. Adding the geoid changes to the mass change signal induced by the tide gives the amplitude of the geocentric sea level response to the nodal cycle, as is given in Figure 7, which should be used to correct altimetry. The geoid response to the nodal cycle is less than 10% of the nodal cycle load.

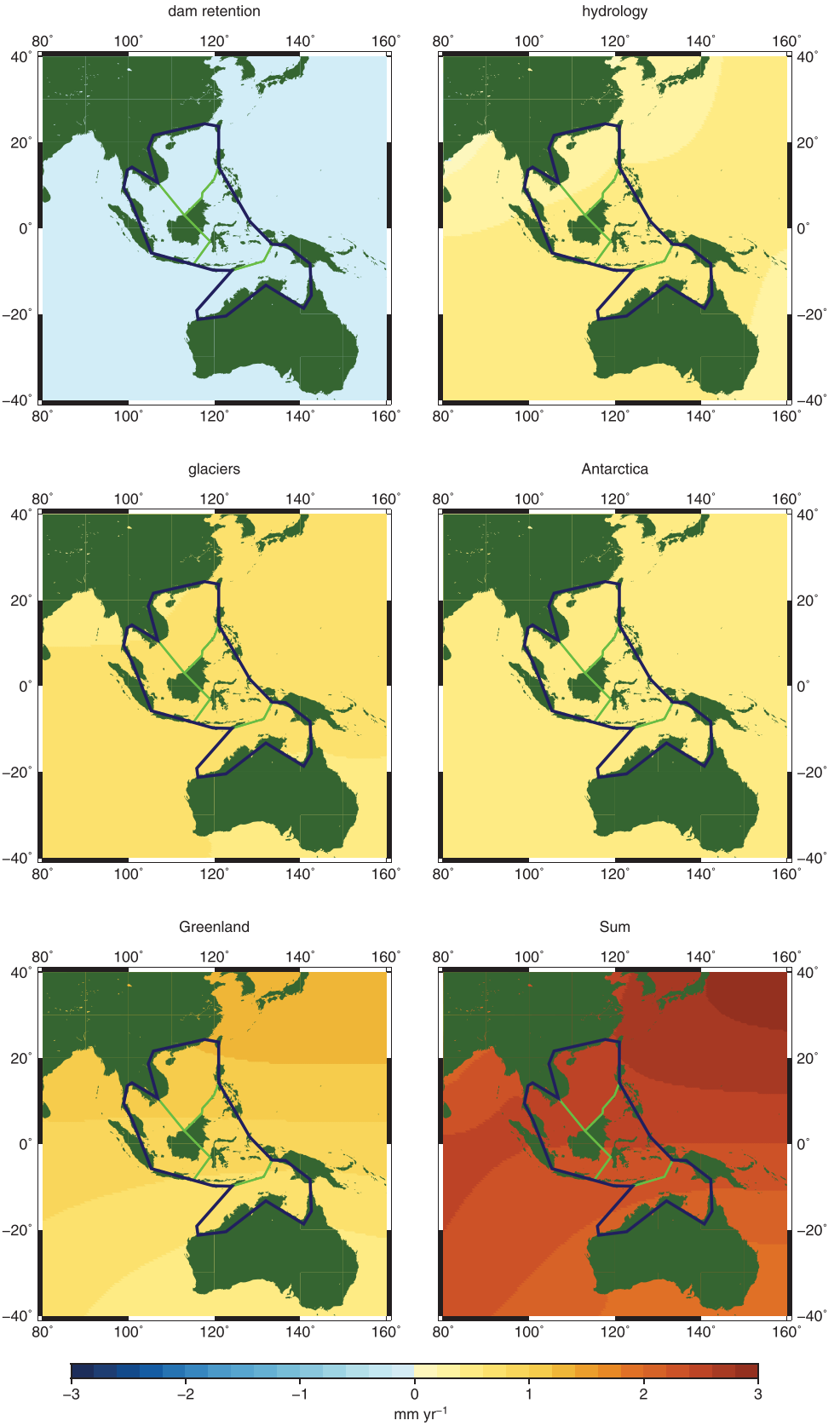

Figure 6. Absolute sea level trends between January 2005 and December 2012 computed from five present-day mass change contributions. In the last figure the sum of all contributions.

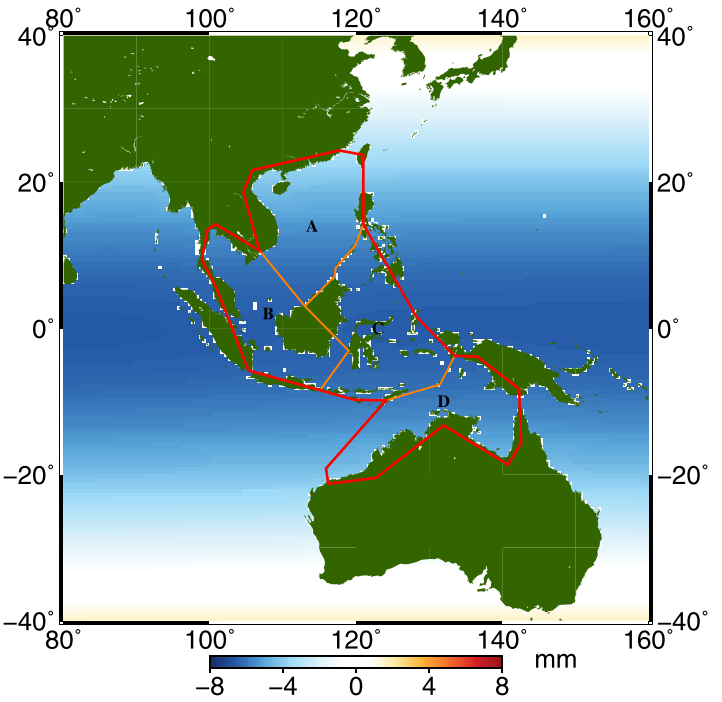

Figure 7. Amplitude of the Nodal cycle in the TAS region. Positive values correspond to a peak in the nodal cycle in 2006. Negative amplitudes indicated a minimum in 2006.

4. Results

First, we compare the statistically weighted time series from section 3.4 with the unweighted time series from GRACE, altimetry, and the reanalyses. Then we discuss the behavior of mass and steric sea level in the four TAS regions. In section 4.2 we remove the semiannual and annual cycles and we relate steric sea level and mass to the two PCs of wind stress and Dipole Mode Indices (DMI). In section 4.3, we regress the steric and mass components on to PC1, PC2, and DMI to examine possible oceanic influences on the estimated trends. In addition for the mass component, we will relate the trends to the nodal cycle and absolute sea level trends obtained from mass redistribution fingerprints. Last, the TAS contribution to GMSL rise is estimated.

4.1. Time Series

In this section we compare the unweighted and statistically weighted (equation (15)) mass and steric time series and describe their variability in each TAS region.

4.1.1. Statistically Weighted Time Series

In Figure 8 time series of mass, steric, and total sea level for the four regions are given. The seasonal cycle of the total sea level is captured by both methods (altimetry and GRACE + reanalyses) in the South China Sea region. When the two methods differ, the statistical optimal time series tends to lie between the two time series. This suggests that the error bars of altimetry and GRACE + reanalyses are on the same order of magnitude. The GRACE mass time series shows a more pronounced annual cycle than altimetry-reanalyses, which appears to be noisier. In the South China Sea region, the reanalysis sea level estimates do not correlate well with the altimetry measurements [*Balmaseda et al.*, 2013; *Zuo et al.*, 2015] and the noise of the altimetry-reanalysis time series is relatively large. The statistical-weighted time series therefore follows more closely the GRACE time series. Both steric sea level time series (reanalysis and altimetry-GRACE) already matched well, so the statistically weighted one overlaps with both. Note that there are some Argo floats present in this region that help to constrain the reanalysis products.

In the Thailand-Java region, total sea level estimated from GRACE + reanalyses departs from altimetry in the first 3 years of the time series. This is caused by the effect of postseismic deformation of the Earth due to the Sumatra-Andaman earthquake, despite the correction that has been applied. The statistically weighted mass time series for the region closely follows GRACE at the end of the time series, but the opposite is true in the first 3 years, as a consequence of the increased error in GRACE mass estimates as described in section 3.2.2. The statistically weighted steric signal in the bottom plot for Thailand-Java follows the reanalyses, because the altimetry-GRACE steric time series is relatively noisy. We must note that large fresh water fluxes from the Mekong might also reduce the quality of reanalyses steric sea level estimates, because they are poorly constrained due to a lack of in situ salinity measurements [*Balmaseda et al.*, 2013].

In the seas of Banda-Celebes, both altimetry and GRACE + reanalyses capture the interannual and annual signals. The statistically weighted time series closely resembles the altimetry time series, because it has relatively small error bars due to short correlation scales. Mass is fully explained by GRACE, so altimetry-reanalyses has barely any influence on the statistically weighted time series. The statistically weighted steric

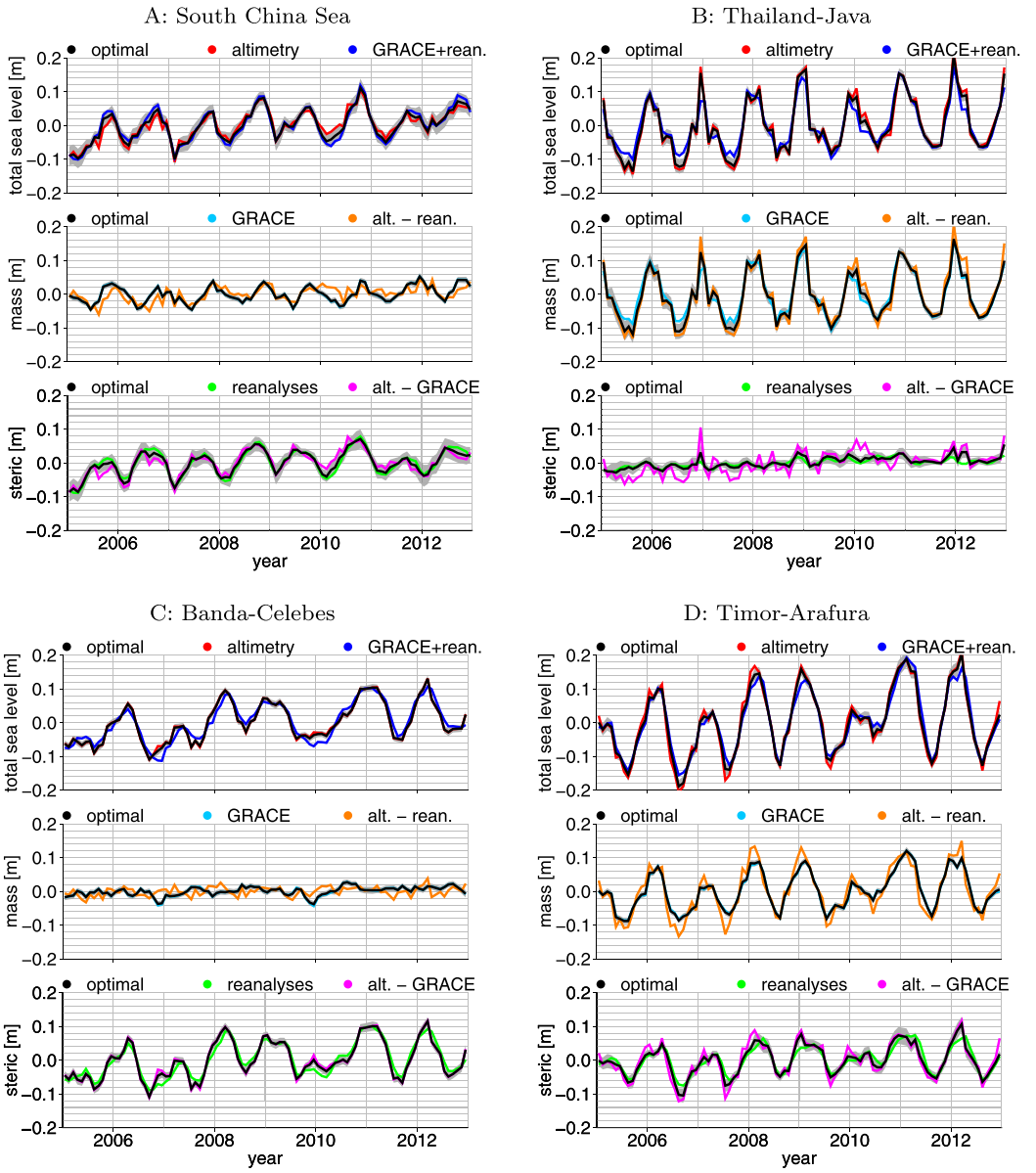

Figure 8. Time series of total and steric sea level and mass for the four regions with the annual cycle retained. In this figure, the term "reanalyses" indicates the steric sea level obtained from reanalyses, in order to avoid confusion with the term "steric" used to indicate statistically weighted steric sea level. (top) Total sea level from altimetry in red, from GRACE + reanalyses in blue, and the optimal solution in black. (middle) Mass from GRACE in light blue, from steric-corrected altimetry in orange, and the optimal solution in black. (bottom) Steric sea level from the reanalyses in green, from altimetry-GRACE in purple, and the optimal solution in black.

signal is primarily constrained by altimetry-GRACE, due to larger discrepancies between reanalyses compared to the previous two regions, which inflates the error.

In the Timor and Arafura seas, the interannual variability appears to be captured by all-time series, but there are discrepancies in the annual cycle. There are substantial observable differences in the annual cycle of mass. The weighted time series for the mass signal closely resembles the GRACE time series, because the errors on the altimetry-reanalyses time series are larger. With the exception of a few peaks, we observe only minor differences between the steric sea level time series. The statistically weighted steric sea level time series is closer to altimetry-GRACE than the reanalyses.

4.1.2. Mass and Steric Variability

Sea level variability in the South China Sea is dominated by the steric component (Figure 8) and as demonstrated in section 3.3 this primarily reflects changes in temperature. There is also an annual signal in mass,

but this is approximately a factor of two smaller than that of the steric signal, which is several centimeters in amplitude.

Much larger annual cycles in sea level are found in the Thailand-Java region of approximately a decimeter. In contrast with the South China Sea, the largest fraction of the variability is the mass component, indicating a seasonal mass flux component into this basin. The seasonal steric component is weak because the region is shallow, which limits thermal expansion, and temperature changes are small over the year, which is evident in the sea surface temperature [*Knudsen et al*., 1996].

The sea level time series of the deeper Banda-Celebes region exhibit a less pronounced annual cycle than Thailand-Java. The annual cycle in steric sea level is however larger than that of Thailand-Java, but the annual cycle in sea surface temperature is comparable as shown by *Knudsen et al*. [1996]. Since the water column is deeper it is able to expand more in response to comparable heating than the Thailand-Java region. The interannual variability is primarily caused by the steric signal as well.

The highest sea level variability in the TAS occurs in the Timor and Arafura seas, which are deeper than Thailand-Java and shallower than the other two regions. The variability is a combination of mass fluctuations and temperature changes. The annual cycle in sea level in this region is among the highest in the world [*Vinogradov et al*., 2008]. The annual cycle in the steric time series is several centimeters in amplitude and the mass signal is slightly larger. Note that the interannual variations (for example smaller peaks in 2007 and 2010, coinciding with El Niño events) in the steric and mass signals is comparable. Additionally, the steric time series in Banda-Celebes strongly resembles the mass time series of Timor-Arafura. This suggests that there is a dynamic coupling between the two regions, perhaps as a consequence of the large steric sea level fluctuations in Banda-Celebes [*Landerer et al*., 2007; *Bingham and Hughes*, 2012], or the signals have the same driver. In the following section, this will be discussed further.

4.2. Interannual Variability

We next consider possible drivers of interannual sea level variability in the TWS by regressing steric and mass components on to equatorial wind stress (PC1 and PC2) and processes associated with the DMI. In Figure 9, we show the PC1, PC2 of the equatorial wind stress, and the DMI regressed through the steric and the mass components. Before regression, the nodal cycle is removed from the mass time series, which is also plotted as a black-dotted line. The trend, the annual and the semiannual signals are regressed together with the indices and removed from the steric and mass time series. In Table 3 we have computed the Coefficients Of Determination (COD) for each of the indices and the sum of them. These CODs represent the ratio of the variances of the regressed index and the mass or steric time series after removing the trend, the nodal, the annual, and the semiannual cycles. The last three columns of Table 3 show the *p*-values of the regressed indices. We also investigate the source of the mass fluctuations in the TAS by looking at correlations with steric sea level in the surrounding oceans.

4.2.1. Regional Effects

For the South China Sea, the region farthest from the equator, only a small fraction of mass and steric sea level is explained by the indices. PC1 and the DMI explain a small fraction of the mass variability and have a significant *p*-value, while PC2 explains a small fraction of the steric variability. Combining the regressed indices shows that only 20% of the variability of the steric signal is explained by PC1, PC2, and the DMI, and that this is even lower for the mass signal. As visible in Figure 9, there is still substantial interannual variability in steric sea level.

In the shallow Thailand-Java region, the steric variability is small compared to the South China Sea. Nevertheless, a substantial fraction (COD of 0.42) of the steric signal is explained by the DMI. The regressed PC1&2 indices are insignificant as indicated by their *p*-values. A negative (at the end of 2006) and a positive peak (at the end of 2010) are visible in the regressed DMI time series in Figure 9, which correspond, respectively, to positive and negative peaks in the DMI of Figure 4. This is in line with *Meyers et al*. [2007], who showed that a positive temperature anomaly, causing a steric response, is present during negative DMI. The mass signal in this area is much larger than the steric signal and it is driven primarily by PC1 for which the COD is 0.55. ENSO, which is in-phase with PC1, appears locally as a steric phenomenon which manifestates itself in the WTPO as a deepening of the thermocline during the La Niña phase and with temperature anomalies above as well as below the thermocline [*Zheng et al*., 2015]. We argue that during the La Niña phase water flows into the shallow areas down a pressure gradient established by a large steric response in

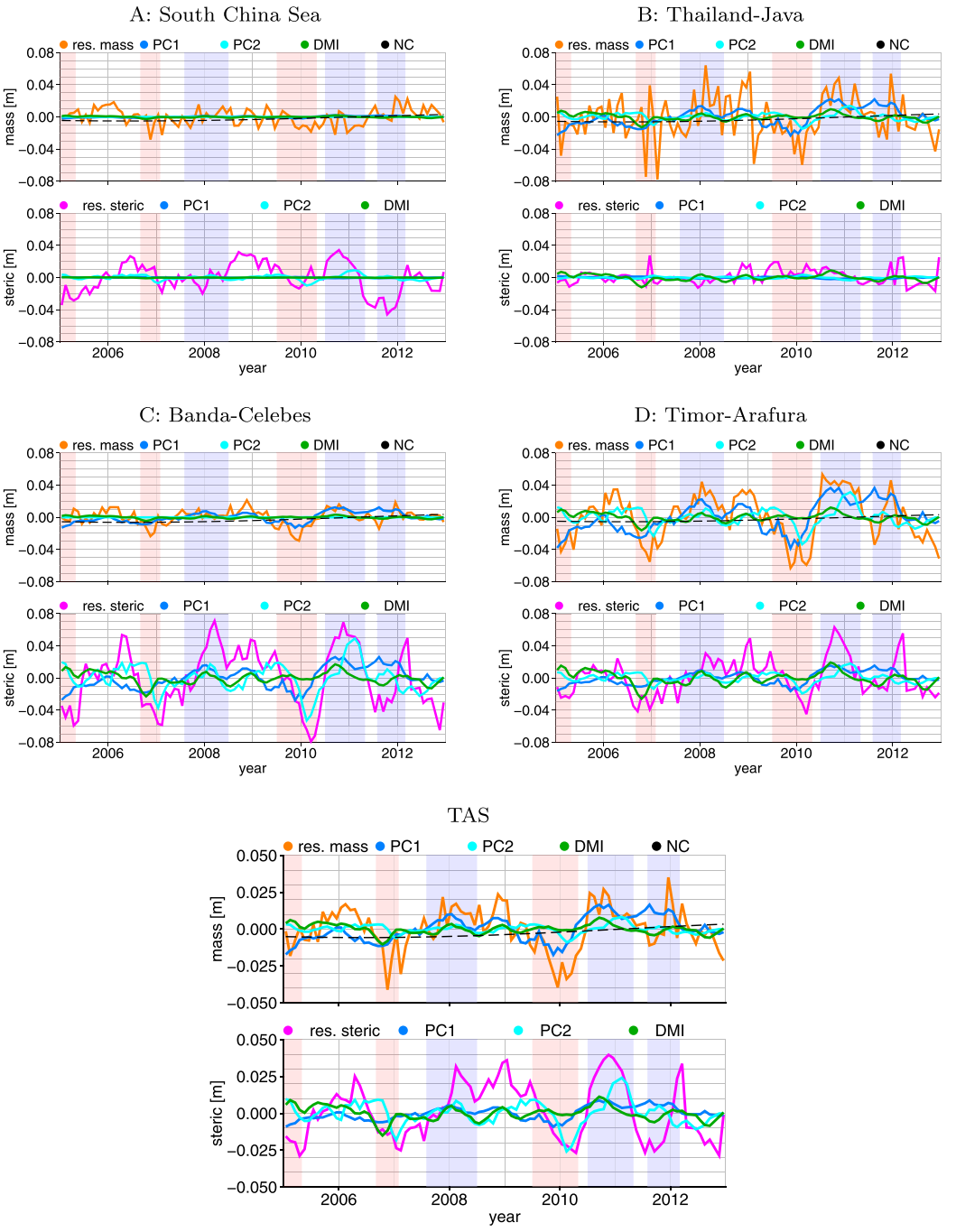

Figure 9. Time series of (top) mass and (bottom) steric sea level between January 2005 and December 2012 with annual and semiannual signals removed. In blue the regression of PC1, in light blue PC2, and in green the DMI. The subtracted nodal cycle is shown as a black-dotted line. The red and blue shades indicate, respectively, El Niño and La Niña states.

surrounding deeper area. We will return to this point in section 4.2.2. The opposite occurs during El Niño. An additional fraction of the interannual variability in the Thailand-Java region is explained by PC2, which suggests that during the recovery phase of La Nina, the mass anomaly is positive. The effects of DMI on the mass in Thailand-Java are small, but still a significant regression coefficient is found.

The Banda-Celebes seas exhibit only small mass variations at interannual time scales, which are most related to PC1. Note that the mass variations are almost in-phase with those of Thailand-Java, but that the regression with PC2 is insignificant. The interannual steric variability is largest in the region, which is

Table 3. Coefficients of Determination for the Indices (Individually and Combined) Regressed Through the Mass and Steric Time Series Between January 2005 and December 2012 for the Four Regions[a]

		COD				*p*-Value		
		PC1	PC2	DMI	Total[b]	PC1	PC2	DMI
Steric	A	0.03	0.19	0.01	0.20	*0.37*	0.00	*0.42*
	B	0.16	0.14	0.42	0.44	*0.12*	*0.06*	0.00
	C	0.53	0.50	0.21	0.70	0.00	0.00	0.00
	D	0.49	0.29	0.37	0.64	0.00	0.00	0.00
	TAS	0.35	0.48	0.27	0.63	0.00	0.00	0.00
Mass	A	0.14	0.01	0.08	0.16	0.03	*0.42*	0.05
	B	0.55	0.18	0.14	0.56	0.00	0.00	0.00
	C	0.77	0.01	0.12	0.77	0.00	*0.44*	0.00
	D	0.82	0.35	0.16	0.84	0.00	0.00	0.00
	TAS	0.73	0.18	0.20	0.73	0.00	0.00	0.00

[a]The regions South China Sea, Thailand-Java, Banda-Celebes, and Timor-Arafura are, respectively, indicated with A, B, C, and D. The last three columns indicate the *p*-value. In italic are the coefficients that are not significantly different from zero based on a 5% significance level.

[b]The column "Total" is the COD of the multilinear regression time series of the three indices, which is not equal to the sum of the individual CODs.

expected as the region is deep, which allows the water column to expand more at equal temperature increases. We find significant regression coefficients for all indices for the steric time series, but most of the signal is explained by PC1 and PC2. Because we find negative regression coefficients (not shown) for both PCs and PC1 is in-phase with the Niño 3.4 index, while PC2 responds just out-of-phase, we argue that the steric signal in Banda-Celebes is slightly delayed with respect to ENSO. The DMI also has an influence (COD of 0.20), which agrees with the temperature patterns found by *Meyers et al*. [2007].

The southernmost Timor-Arafura region exhibits the largest interannual variability, of which mass represents the largest fraction as is visible in Figure 9. All of the regressed indices are significant in this region, as shown by their *p*-values. The individual COD for the regressed PC1 is 0.82, with a negative regression coefficient this means that the mass anomaly is positive when PC1 is negative. Since this is a relatively shallow area, water is expected to move into the Timor-Arafura region at the moment of La Niña from a region with a large steric response, a comparable effect as for the mass signal in Thailand-Java. Note that at the Fremantle tide gauge, located farther south along Australia's west coast, correlations between sea level and ENSO are observed as well [*Feng et al*., 2004]. Also PC2 has a large COD, which means that the water inflow is slightly delayed with respect to ENSO, which is in-phase with PC1. The steric signal in the Timor-Arafura region is in-phase with the mass signal. Table 3 shows that PC1&2 represent a smaller fraction of the steric signal compared to that of the mass and that the DMI is responsible for a large fraction of the variability, although it is still smaller than PC1. Again, this is in line with the sea surface temperature patterns in *Meyers et al*. [2007] as discussed in section 3.3.

4.2.2. Remote Steric Effect

Interannual steric variations summed over the entire TAS correspond primarily to the steric signals in the Banda-Celebes region and the South China Sea. Based on the CODs, PC2 is responsible for the largest part of the steric signal, which indicates the highest and lowest temperatures are found just after La Niña and El Niño events. Table 3 indicates that we can explain about 63 percent of the steric signal for the whole TAS. The interannual variability of the mass signal, which is primarily linked to the Timor-Arafura and Thailand-Java regions, is slightly smaller, but about 73 percent is explained by the regressed indices of which PC1 represents by far the largest fraction. While the steric signal can be explained by temperature changes of the water within the TAS, a flux of water is required from outside the TAS to account for the mass signal.

In Figure 10 we investigate the origin of the interannual mass fluctuations further. To get a horizontal mass flux in to the TAS from outside the region, we hypothesize that steric sea level fluctuations are higher outside the TAS than within, which result in a pressure gradient and mass exchange, which we call the remote steric effect. Therefore, steric sea level in the surrounding regions of the TAS is computed from interpolated Argo grids [*Roemmich and Gilson*, 2009] (so that they are independent from the reanalyses used in this study) as is done in section 3.3, from a reference depth of 1500 dBar. We then compute the difference of steric sea levels in the surrounding regions at each grid point with the mean steric sea level in the TAS. The correlation of these steric sea level differences with the mass time series in the TAS is depicted in the top-left plot of Figure 10. We find a

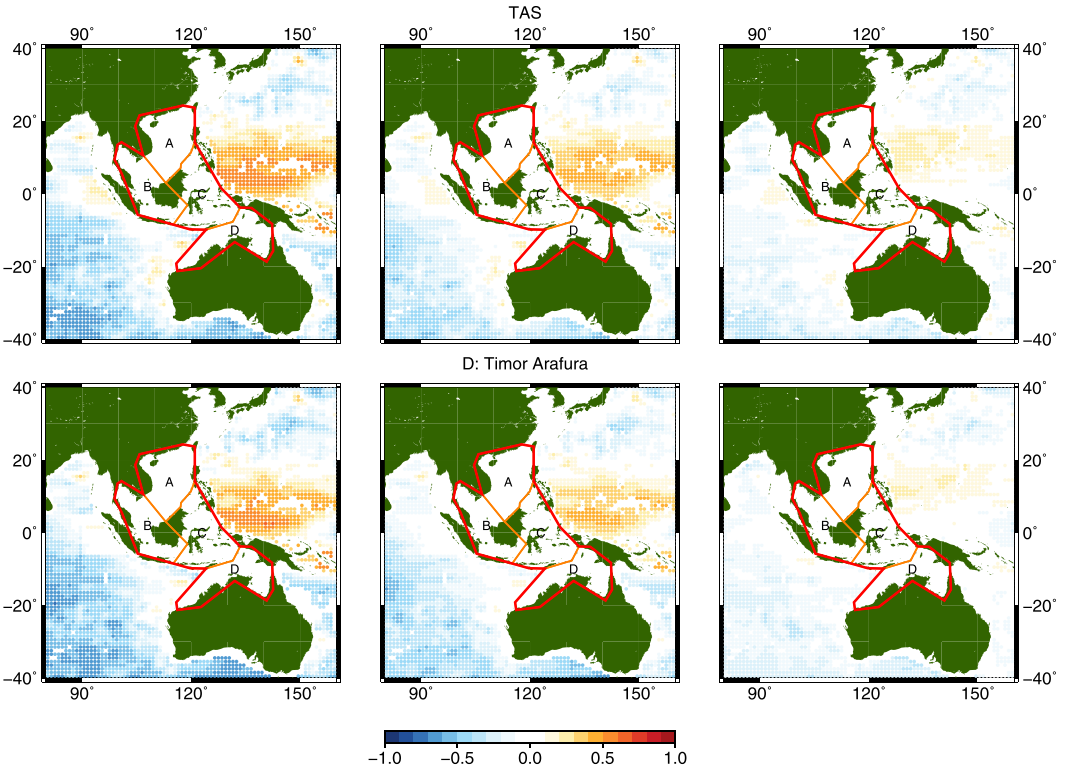

Figure 10. Correlation of relative steric sea level (i.e., the steric sea level minus the mean steric sea level in the TAS), surrounding the TAS with the mass in the TAS. (left) Full signal. (middle) PC1 removed. (right) PC1&2 removed.

significant correlation across a large section of the WTPO, indicating that the steric build up in this region drives a mass flux in to the TAS. A small region of high correlation appears near the equator in the Indian Ocean, which may be associated with DMI-related fluctuations. We repeat the calculation using mass from the Timor-Arafura region, where the mass component is strongest, instead of the entire TAS. We find a similar correlation pattern as for the entire TAS (bottom-left plot, Figure 10), but with weaker correlations with the Indian Ocean steric variations, as expected from the lower COD. Comparable, but slightly weaker correlation patterns are found for the Banda-Celebes and Thailand-Java regions (not shown). For the South China Sea, we find correlations of maximally 0.4 in the WTPO, but the patterns look significantly different (not shown).

To confirm that ENSO is the principal driver of steric sea level variations in the region, we repeat the analysis but regress and remove PC1 (middle plots, Figure 10), and PC1 and PC2 from the steric height differences (right plots, Figure 10). For the whole TAS, correlations with PC1 removed are reduced from 0.6–0.7 to 0.4–0.5 in the WTPO. For the Timor-Arafura region, the correlation is even further reduced to typically around 0.3–0.4 in the WTPO. Reductions in correlation by removing PC1 are also present when considering the mass signals in Thailand-Java and Banda-Celebes regions, but barely for the South China Sea (not shown).

The correlations drop considerably lower ($<$0.2) with the inclusion of PC2 (right plots, Figure 10). For the Timor-Arafura seas comparison, correlations are near zero across the WTPO. Similar results are found for the mass in Thailand-Java, while for the Banda-Celebes region a substantial amount of correlation is still present. After removing PC1&2 from the relative steric sea level, the correlation between mass in the South China Sea is virtually unchanged.

In conclusion, mass changes in the TAS are linked to steric sea level changes in the WTPO. The steric changes in the WTPO are driven by ENSO. Both PCs of the equatorial wind stress are required to remove the largest part of the correlation between mass in the TAS and WTPO. Since PC2 is required, it appears that the dynamic response of the mass is slightly delayed with respect to El Niño and La Niña. Only the mass signal in the South China Sea appears to be decoupled from the first two PCs of the equatorial wind stress.

Table 4. Steric Sea Level Trends in mm yr^{-1}[a]

	Total	Ind Rem.	PC1	PC2	DMI
A	5.3 ± 0.5	5.4 ± 0.6	0.1	0.1	0.0
B	4.3 ± 0.3	4.8 ± 0.4	0.2	−0.0	0.3
C	9.6 ± 0.3	8.2 ± 0.4	−2.9	0.7	0.5
D	4.5 ± 0.4	4.5 ± 0.4	−1.7	0.3	0.6
TAS	6.4 ± 0.3	6.1 ± 0.4	−1.0	0.3	0.3

[a]The four regions South China Sea, Thailand-Java, Banda-Celebes and Timor-Arafura are respectively indicated with A, B, C and D. The second column "Total" shows the trend without regressing the indices. The fourth column "Ind rem." show the trend with regressing the indices. In the last three columns, we indicate the regression trends of the indices.

4.3. Trends

Interannual ocean dynamics strongly affect trends computed from short time series and the estimated trends therefore do not provide a proper indication for what happens to sea level on time-scales longer than the considered 8 years. We therefore investigate the effects of including indices of ocean dynamics in the regression on the estimated trend from the statistically weighted steric and mass time series. The trends and their errors are computed using weighted least squares, by propagating the errors obtained from equation (16) in section 3.4. For the mass time series specifically, we also take into account the nodal cycle. Eventually for the mass time series, we compare the trends after removing the nodal cycle and with the regression of the indices to those obtained from mass redistribution fingerprints. In Table 4 the estimated steric sea level trends are given, which are computed over the period January 2005 to December 2012. The same is performed for the mass trends and those are given in Table 5. In the last three columns, the "negative" regression trends for the three indices are provided, to give an indication how indices affect the trends. A positive value for the regression trends therefore indicates a positive effect on the estimated trend. The regression trends are computed with ordinary least squares through the PC1, PC2, and DMI regression time series, as given in Figure 9. Summing them gives a different value than the difference between the trends regressed with and without indices, because correlations are not taken into account.

4.3.1. Regional Trends

The total steric trend in the South China Sea of 5.3 mm yr^{-1} is about twice as large as the mass trend of 2.8 mm yr^{-1}. By removing the contribution of the nodal cycle, the mass trend reduces by 1.2 mm yr^{-1}. Both tables indicate that the effect of regressing indices has minimal effect on the estimated mass and steric sea level trends in the South China Sea region. This is expected, because the CODs of the time series of the indices, given in Table 3, are only 0.20 and 0.16.

In the shallow Thailand-Java region, comparable trends are found for mass and steric sea level between 4 and 5 mm yr^{-1}. The nodal cycle reduces the mass trend to 3.4 mm yr^{-1}. While the steric sea level trend increases by regression with the indices, primarily as a result of the DMI, the mass trend decreases further due to PC1. The negative effect of PC1 on the trend is the compensation for the high amplitude La Niña event relatively late in the time series [*Boening et al.*, 2012], which affects the mass in Thailand-Java area as discussed in the previous section. PC2 and the DMI have a small positive effect on the mass trends.

The Banda-Celebes seas exhibit by far the largest steric sea level trend in the TAS, even after the regression with the indices. It is again the negative trend of PC1 that causes this reduction, while part of the trend is

Table 5. Mass Trends in mm yr^{-1}[a]

	Total	NC rem.	Ind rem.	FP	PC1	PC2	DMI
A	2.8 ± 0.2	1.8 ± 0.2	1.6 ± 0.2	2.5	−0.2	0.0	0.1
B	4.9 ± 0.4	3.4 ± 0.4	2.3 ± 0.5	2.4	−2.5	0.2	0.3
C	2.5 ± 0.2	1.2 ± 0.2	−0.1 ± 0.2	2.4	−1.4	−0.0	0.1
D	7.7 ± 0.2	6.6 ± 0.2	3.6 ± 0.3	2.2	−4.1	0.5	0.4
TAS	4.5 ± 0.2	3.1 ± 0.2	2.0 ± 0.2	2.4	−1.8	0.1	0.2

[a]The four regions South China Sea, Thailand-Java, Banda-Celebes, and Timor-Arafura are, respectively, indicated with A, B, C, and D. The second column "Total" shows the trend without regressing the indices. The third column "NC rem." provides the trend after removing the nodal cycle. The fourth column "Ind rem." shows trends after removal of the nodal cycle and with regression of the indices. In the fifth column "FP," the estimated trends from mass redistribution fingerprints are given. In the last three columns, we indicate the regression trends of the indices.

recovered by the other two indices. In contrast to steric sea level, the mass component exhibits the smallest trend of the four regions. After removing the nodal cycle and regressing with the indices, there is no significant mass trend left.

In the Timor-Arafura region, a larger mass than steric trend is present. After the removal of the nodal cycle, the mass trend still remains significantly (two standard deviations) larger than the steric trend. The ocean dynamics have no influence on the steric trend, because PC2 and the DMI compensate loss of trend caused by the regression of PC1. The mass trend is reduced to 3.6 mm yr^{-1} by regressing indices, which remains the largest mass trend in the TAS.

The steric trend averaged over the whole TAS is about 2 mm yr^{-1} larger than the mass trend. There is a insignificant reduction of the steric trend to 6.1 mm yr^{-1} when the indices are regressed. Removal of the nodal cycle and regression of the indices lowers the mass trend to 2.0 mm yr^{-1}, about one-third of the remaining steric trend.

4.3.2. Comparison to Mass Redistribution Fingerprints

Once the major ocean dynamic signals (PC1&2 and DMI) are removed, the residual mass trends are compared to the sum of the mass fingerprints. The mass redistribution fingerprint trends for the individual regions are given in the fifth column "FP" of Table 5. For the whole TAS, the yearly sea level time series of the mass redistribution fingerprints are shown in Figure 11. As visible in the figure, the trend of the fingerprints is close (within the 95% confidence interval) to the observed change Table 5. Based on this correspondence, we infer that the net flux of water mass, after removing all the ocean dynamics and mass redistribution effects, through the boundaries of the TAS is statistically insignificant. Table 5 shows that there is a positive discrepancy with respect to the fingerprints in the shallow Timor-Arafura region and negative discrepancies in the deep regions. Since the water influx into the TAS is statistically insignificant, this suggests mass exchange between the deep and shallow regions within the TAS, especially between Banda-Celebes and Timor-Arafura.

Time series of the individual fingerprints (Figure 11, bottom plot) show that. Over the considered time period, Greenland ice loss is the largest contributor to mass trends in the region, followed by glacier melt. Not only does the Greenland ice sheet have the largest mass loss, but its location far away from the TAS increases the contribution with respect to the glaciers and Antarctic melt. Furthermore, while the glaciers contribute spatially quite homogeneously to the trends in the TAS (Figure 6), the contributions of Antarctica and Greenland vary primarily from north to south. The meridional gradient of the Greenland fingerprint is

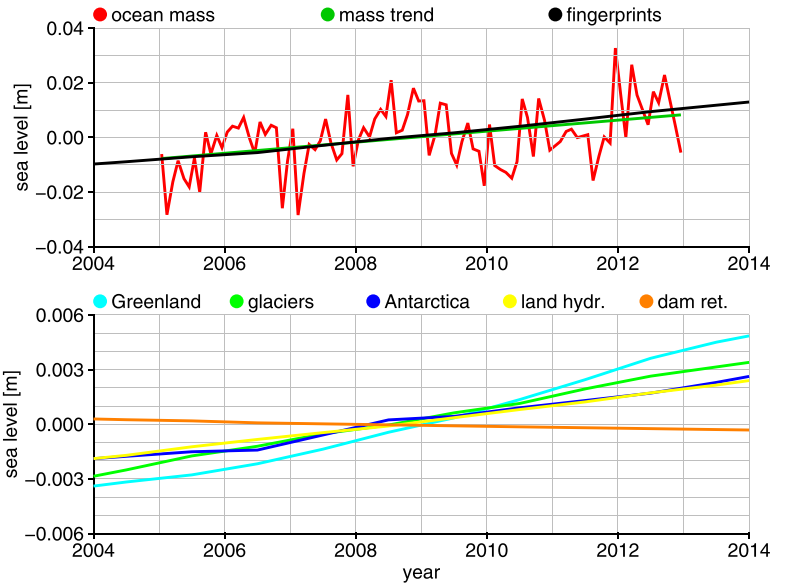

Figure 11. (top) In red the sea level time series (m) for the whole TAS region, after removing the contributions of the regressed PC1&2 and DMI indices, the nodal cycle and the annual and semiannual cycles. In black the sum of the mass fingerprints. (bottom) The fingerprint time series of Greenland, glaciers, Antarctica, dam retention and land hydrology respectively in light blue, green, blue, yellow, and orange.

Table 6. Contribution to GMSL over January 2005 to December 2010 in mm yr^{-1}[a]

	TAS Only	TAS-Global	Global Contr.
Sum	12.4	10.7	0.3
Steric	8.2	8.1	0.2
Mass	4.2	2.6	0.1

[a]The first column contains the trends in the TAS. The second column contains the relative trends with respect to the global estimates. The last column shows the contribution to the global budget.

particularly evident, with a 0.3 mm/yr difference between the South China Sea and the Timor-Arafura regions.

4.4. Contribution to Global Mean Sea-Level Rise

To determine the contribution of the TAS to global sea level, we first estimate the global mean mass and steric sea level trends. Then the differences between the TAS trends and the global trends are computed. An estimate of the contribution of the differenced trends $\Delta t_{relative}$ is then computed using the ratio between the surface area A_{TAS} of the TAS and the rest of the oceans $A_{global} - A_{TAS}$, such that:

$$\Delta t_{global} = \frac{A_{TAS}}{A_{global} - A_{TAS}} \Delta t_{relative}, \tag{21}$$

is the effect of including the TAS into global ocean budgets. This approach is applied for both the mass and the steric components.

The global mean steric sea level and global mean mass time series are obtained from the NASA website [*Llovel et al.*, 2014; *Watkins et al.*, 2015]. The global mean steric sea level is computed from Scripps temperature and salinity grids [*Roemmich and Gilson*, 2009], in which the TAS region is completely excluded. A $3^\circ \times 3^\circ$ mascon solution is used to construct the global mean mass time series, which includes several cells within the TAS region. Since the effect of the mass in the TAS on the global mean mass trend is only a fraction of the mass trend in the TAS itself, this will not significantly affect the outcome of the computation. The time series trends are computed between January 2005 and December 2010 for comparison with other studies, which results in 0.1 mm yr^{-1} for the steric trend and 1.6 mm yr^{-1} for the mass trend. The trends over the period January 2005 to December 2012 are comparable to the trend over the shorter period.

The TAS trends derived from the statistically weighted time series are 8.2 mm yr^{-1} for the steric component, and 4.2 mm yr^{-1} for the mass component (Table 6, Col. 1). Taking the difference between the TAS and global trends estimated above (Table 6, Col. 2), we compute that the TAS contribution is 0.2 mm yr^{-1} for global steric and 0.1 mm yr^{-1} for global mass. Because the ratio of the surface area of the TAS and the global ocean is small, the error bars on the contribution to the global estimates are small and therefore they are not provided in the table.

Based on the ORAS4 reanalyses, *Dieng et al.* [2015] estimated that the global mean steric sea level is underestimated by approximately 0.25 mm yr^{-1} over the period January 2005 to December 2013. Even though we computed the value over a slightly shorter period, our estimate of 0.2 mm yr^{-1} is close to this value. They did however not discuss the effect of the 300 km cut off from the coast in GRACE global mass, which was based on the time series of *Johnson and Chambers* [2013]. A 300 km cutoff effectively removes the whole TAS contribution from the global solution. We estimate that excluding the TAS in global mass estimates causes underestimation of 0.1 mm yr^{-1}. Combining both numbers gives a trend of 0.3 mm yr^{-1}, which is consistent with the 0.5 ± 0.2 mm yr^{-1} computed by *Von Schuckmann et al.* [2014].

5. Conclusions

For the first time satellite altimetry, satellite gravimetry and reanalysis data are used to determine the steric and mass components of sea level variations in the TAS. To study the sea level variability in the TAS in more detail, time series of the sea level components are computed for four regions. The uncertainties of the time series of total sea level from altimetry, mass from GRACE, and steric sea level from reanalyses are used to derive a statistically optimal separation between the steric and mass components. The statistically weighted time series are used to study the interannual variability and trends in the TAS, as well as their contribution to global mean sea level.

The largest variability in steric sea level is found in the deeper areas as the South China Sea and the Banda-Celebes seas. The small water column of the Thailand-Java and Timor-Arafura regions is not able to expand as far as the other two. In contrast, the largest mass signals are present in the shallower regions. We argue that this is a dynamical response to larger steric sea level fluctuations in neighboring areas.

Regression with the first two PCs of the equatorial Pacific wind stress and the DMI showed that the South China Sea largely is unaffected by ENSO and Indian Ocean dipole dynamics. The steric sea level in the Banda-Celebes and Timor-Arafura seas is strongly driven by PC1&2, which are used to represent wind forcing that is either in phase with ENSO (PC1), or peaked around the southward shift of anomalous winds (PC2). The DMI has a small effect on the temperatures in Thailand-Java and causes a substantial fraction of (thermo-)steric variability in Timor-Arafura. Mass signals in the shallow areas are almost 180 degrees out-of-phase with PC1. PC2 shows a strong contribution, especially in the Timor-Arafura region. We believe that the shallow region mass changes, which dominate the total mass change in the TAS, are due to net transport from the neighboring WTPO to the shallow regions associated with variations in WTPO steric sea level, which are related to PC1&2.

Accounting for interannual variations associated with the PC1, PC2, and DMI indices impacts the estimation of linear trends. Regressing PC2 and the DMI have over the whole TAS a slight positive effect on the mass and steric trends, while regressing PC1 reduces the trends. This leads to a reduction in mass and steric trends. The mass trends are also affected by the nodal cycle, because it causes a mass change with a minimum in 2006 and a maximum in 2015. Trends are decreased with approximately 1.3 mm yr^{-1} when correcting for the nodal cycle.

The mass trend over the whole TAS is statistically equal to the trend estimated from mass redistribution fingerprints. However, within the four regions there are differences: the deep regions have smaller mass trends than their fingerprint estimates, while in the Timor-Arafura region we find larger trends than its fingerprint. We argue that there is an internal redistribution of water within the TAS, where water flows from deep regions with a large steric response into the shallower regions.

Finally, we computed trends for the whole TAS and estimated the contribution to the global budgets. Omitting the TAS results in an underestimation of the mass and steric components with 0.1 and 0.2 mm yr^{-1}, respectively. These numbers are in line with previous studies.

Our approach for separating mass and steric contributions to sea level changes can be applied to other basins where Argo float coverage is limited, such as the Caribbean Sea, the Gulf of Mexico, and the Yellow Sea. To investigate the drivers of mass and steric sea level variability, appropriate indices should be used.

Acknowledgments
This study is funded by the Netherlands Organisation for Scientific Research (NWO) through VIDI grant 864.12.012 (Multi-Scale Sea Level (MuSSeL)). The RADS altimetry data are obtained from: http://rads.tudelft.nl/rads/rads.shtml. The ITSG-Grace2016 gravity fields are obtained from: https://www.tugraz.at/institute/ifg/downloads/gravity-field-models/itsg-grace2016/. All reanalysis data are found at: https://reanalyses.org/ocean/overview-current-reanalyses. Scripps temperature and salinty grids interpolated from Argo float measurements: http://www.argo.ucsd.edu/Gridded_fields.html. ERA-Interim wind speed data are downloaded from: http://apps.ecmwf.int/datasets/data/interim-full-moda/levtype=sfc/. SSALTO/DUACS multimission altimetry grids are downloaded from: https://www.aviso.altimetry.fr/en/data/product-information/information-about-mono-and-multi-mission-processing/ssaltoduacs-multimission-altimeter-products.html.

References

Ablain, M., et al. (2015), Improved sea level record over the satellite altimetry era (1993–2010) from the Climate Change Initiative Project, *Ocean Sci.*, *11*, 67–82.

Andersen, O. B., P. Knudsen, and L. Stenseng (2015), The DTU13 MSS (Mean Sea Surface) and MDT (Mean Dynamic Topography) from 20 Years of Satellite Altimetry, in *International Association of Geodesy Symposia*, pp. 1–10, Springer, Cham, Switzerland, doi:10.1007/1345_2015_182.

Balmaseda, M. A., K. Mogensen, and A. T. Weaver (2013), Evaluation of the ECMWF ocean reanalysis system ORAS4, *Q. J. R. Meteorol. Soc.*, *139*(674), 1132–1161.

Behringer, D. W., and Y. Xue (2004), Evaluation of the global ocean data assimilation system at NCEP: The Pacific Ocean, in *Proceedings of Eighth Symposium on Integrated Observing and Assimilation Systems for Atmosphere, Oceans, and Land Surface*, AMS 84th Annual Meeting, Seattle, Wash.

Bingham, R. J., and C. W. Hughes (2012), Local diagnostics to estimate density-induced sea level variations over topography and along coastlines, *J. Geophys. Res.*, *117*, C01013, doi:10.1029/2011JC007276.

Boening, C., J. K. Willis, F. W. Landerer, R. S. Nerem, and J. Fasullo (2012), The 2011 La Niña: So strong, the oceans fell, *Geophys. Res. Lett.*, *39*, L19602, doi:10.1029/2012GL053055.

Broerse, T., R. Riva, W. Simons, R. Govers, and B. Vermeersen (2015), Postseismic GRACE and GPS observations indicate a rheology contrast above and below the Sumatra slab, *J. Geophys. Res. Solid Earth*, *120*, 5343–5361, doi:10.1002/2015JB011951.

Carton, J. A., and B. S. Giese (2008), A reanalysis of ocean climate using Simple Ocean Data Assimilation (SODA), *Mon. Weather Rev.*, *136*(8), 2999–3017.

Cazenave, A., and G. Le Cozannet (2013), Sea level rise and its coastal impacts, *Earth's Future*, *2*, 15–34.

Chaussard, E., F. Amelung, H. Abidin, and S. H. Hong (2013), Sinking cities in Indonesia: ALOS PALSAR detects rapid subsidence due to groundwater and gas extraction, *Remote Sens. Environ.*, *128*, 150–161.

Dieng, H. B., A. Cazenave, K. von Schuckmann, M. Ablain, and B. Meyssignac (2015), Sea level budget over 2005–2013: Missing contributions and data errors, *Ocean Sci.*, *11*(5), 789–802.

Einarsson, I., A. Hoechner, R. Wang, and J. Kusche (2010), Gravity changes due to the Sumatra-Andaman and Nias earthquakes as detected by the GRACE satellites: A reexamination, *Geophys. J. Int.*, *183*(2), 733–747.
England, M. H., S. McGregor, P. Spence, G. A. Meehl, A. Timmermann, W. Cai, A. S. Gupta, M. J. McPhaden, A. Purich, and A. Santoso (2014), Recent intensification of wind-driven circulation in the Pacific and the ongoing warming hiatus, *Nat. Clim. Change*, *4*(3), 222–227.
Farrell, W. E., and J. A. Clark (1976), On postglacial sea level, *Geophys. J. Int.*, *46*(3), 647–667.
Feng, M., Y. Li, and G. Meyers (2004), Multidecadal variations of Fremantle sea level: Footprint of climate variability in the tropical Pacific, *Geophys. Res. Lett.*, *31*, L16302, doi:10.1029/2004GL019947.
Feng, W., M. Zhong, and H. Xu (2012), Sea level variations in the South China Sea inferred from satellite gravity, altimetry, and oceanographic data, *Sci. China Earth Sci.*, *55*(10), 1696–1701.
Fenoglio-Marc, L., R. Rietbroek, S. Grayek, M. Becker, J. Kusche, and E. Stanev (2012), Water mass variation in the Mediterranean and Black Seas, *J. Geodyn.*, *59*, 168–182.
Ferry, N., L. Parent, G. Garric, B. Barnier, and N. C. Jourdain (2010), Mercator global Eddy permitting ocean reanalysis GLORYS1V1: Description and results, *Mercator Ocean Q. Newsl.*, *36*, 15–27.
Forget, G., J. M. Campin, P. Heimbach, C. N. Hill, R. M. Ponte, and C. Wunsch (2015), ECCO version 4: An integrated framework for non-linear inverse modeling and global ocean state estimation, *Geosci. Model Dev.*, *8*(10), 3071–3104.
Frederikse, T., R. Riva, M. Kleinherenbrink, Y. Wada, M. Broeke, and B. Marzeion (2016), Closing the sea level budget on a regional scale: Trends and variability on the Northwestern European continental shelf, *Geophys. Res. Lett.*, *43*,10,864–10,872, doi:10.1002/2016GL070750.
Hetland, E. A., and B. H. Hager (2006), The effects of rheological layering on post-seismic deformation, *Geophys. J. Int.*, *166*(1), 277–292.
IOC, SCOR, and IAPSO (2010), *The International Thermodynamic Equation of Seawater-2010: Calculation and Use of Thermodynamic Properties*, Intergovernmental Oceanogr. Comm., Manuals and Guides No. 56, 196 p., UNESCO, Paris, France.
Johnson, G. C., and D. P. Chambers (2013), Ocean bottom pressure seasonal cycles and decadal trends from GRACE Release-05: Ocean circulation implications, *J. Geophys. Res. Oceans*, *118*, 4228–4240, doi:10.1002/jgrc.20307.
Klees, R., E. A. Revtova, B. C. Gunter, P. Ditmar, E. Oudman, H. C. Winsemius, and H. H. G. Savenije (2008), The design of an optimal filter for monthly GRACE gravity models, *Geophys. J. Int.*, *175*(2), 417–432.
Kleinherenbrink, M., R. Riva, and Y. Sun (2016), Sub-basin-scale sea level budgets from satellite altimetry, Argo floats and satellite gravimetry: A case study in the North Atlantic Ocean, *Ocean Sci.*, *12*(6), 1179–1203.
Klinger, B., T. Mayer-Gürr, S. Behzadpour, M. Ellmer, A. Kvas, and N. Zehentner (2016), The new ITSG-Grace2016 release, EGU General Assembly 2016, Vienna, Austria.
Knudsen, P., O. B. Andersen, and T. Knudsen (1996), ATSR sea surface temperature data in a global analysis with TOPEX/POSEIDON altimetry, *Geophys. Res. Lett.*, *23*(8), 821–824.
Köhl, A. (2015), Evaluation of the GECCO2 ocean synthesis: Transports of volume, heat and freshwater in the Atlantic, *Q. J. R. Meteorol. Soc.*, *141*(686), 166–181.
Landerer, F. W., J. H. Jungclaus, and J. Marotzke (2007), Ocean bottom pressure changes lead to a decreasing length-of-day in a warming climate, *Geophys. Res. Lett.*, *34*, L06307, doi:10.1029/2006GL029106.
Lee, T., and M. J. McPhaden (2008), Decadal phase change in large-scale sea level and winds in the Indo-Pacific region at the end of the 20th century, *Geophys. Res. Lett.*, *35*, L01605, doi:10.1029/2007GL032419.
Le Traon, P. Y., G. Dibarboure, and N. Ducet (2001), Use of a high-resolution model to analyze the mapping capabilities of multiple-altimeter missions, *J. Atmos. Oceanic Technol.*, *18*(7), 1277–1288.
Leuliette, E. W., and L. Miller (2009), Closing the sea level rise budget with altimetry, Argo, and GRACE, *Geophys. Res. Lett.*, *36*, L04608, doi:10.1029/2008GL036010.
Leuliette, E. W., and J. K. Willis (2011), Balancing the sea level budget, *Oceanography*, *24*(2), 122–129, doi:10.5670/oceanog.2011.32.
Llovel, W., J. K. Willis, F. W. Landerer, and I. Fukumori (2014), Deep-ocean contribution to sea level and energy budget not detectable over the past decade, *Nat. Clim. Change*, *4*(11), 1031–1035.
McGregor, S., A. S. Gupta, and M. H. England (2012a), Constraining wind stress products with sea surface height observations and implications for Pacific Ocean sea level trend attribution, *J. Clim.*, *25*(23), 8164–8176.
McGregor, S., A. Timmermann, N. Schneider, M. F. Stuecker, and M. H. England (2012b), The effect of the South Pacific convergence zone on the termination of El Niño events and the meridional asymmetry of ENSO*, *J. Clim.*, *25*(16), 5566–5586.
Merrifield, M. A. (2011), A shift in western tropical Pacific sea level trends during the 1990s, *J. Clim.*, *24*(15), 4126–4138.
Merrifield, M. A., and M. E. Maltrud (2011), Regional sea level trends due to a Pacific trade wind intensification, *Geophys. Res. Lett.*, *38*, L21605, doi:10.1029/2011GL049576.
Merrifield, M. A., P. R. Thompson, and M. Lander (2012), Multidecadal sea level anomalies and trends in the western tropical Pacific, *Geophys. Res. Lett.*, *39*, L13602, doi:10.1029/2012GL052032.
Meyers, G., P. McIntosh, L. Pigot, and M. Pook (2007), The years of El Niño, La Niña, and interactions with the tropical Indian Ocean, *J. Clim.*, *20*(13), 2872–2880.
Milne, G. A., and J. X. Mitrovica (1996), Postglacial sea-level change on a rotating Earth: First results from a gravitationally self-consistent sea-level equation, *Geophys. J. Int.*, *126*(3), F13–F20.
Mitchum, G. T. (1998), Monitoring the stability of satellite altimeters with tide gauges, *J. Atmos. Oceanic Technol.*, *15*(3), 721–730.
Mitchum, G. T. (2000), An improved calibration of satellite altimetric heights using tide gauge sea levels with adjustment for land motion, *Mar. Geod.*, *23*(3), 145–166.
Pawlocwicz, P., T. J. McDougall, R. Feistel, And R. Tailleux (2012), An historical perspective on the development of the thermodynamic equation of seawater-2010, *Ocean Sci.*, *8*, 161–174.
Phien-Wej, N., P. H. Giao, and P. Nutalaya (2006), Land subsidence in Bangkok, Thailand, *Eng. Geol.*, *82*(4), 187–201.
Proudman, J. (1960), The condition that a long-period tide shall follow the equilibrium-law, *Geophys. J. Int.*, *3*(2), 244–249.
Pugh, D., and P. Woodworth (2014), *Sea-Level Science: Understanding Tides, Surges, Tsunamis and Mean Sea-Level Changes*, Cambridge Univ. Press, Cambridge, U. K.
Raucoules, D., G. Le Cozannet, G. Wöppelmann, M. De Michele, M. Gravelle, A. Daag, and M. Marcos (2013), High nonlinear urban ground motion in Manila (Philippines) from 1993 to 2010 observed by DInSAR: Implications for sea-level measurement, *Remote Sens. Environ.*, *139*, 386–397.
Rietbroek, R., S. E. Brunnabend, J. Kusche, J. Schröter, and C. Dahle (2016), Revisiting the contemporary sea-level budget on global and regional scales, *Proc. Natl. Acad. Sci. U. S. A.*, *113*(6), 1504–1509.

Rodolfo, K. S., and F. P. Siringan (2006), Global sea-level rise is recognised, but flooding from anthropogenic land subsidence is ignored around northern Manila Bay, Philippines, *Disasters*, *30*(1), 118–139.
Roemmich, D., and J. Gilson (2009), The 2004–2008 mean and annual cycle of temperature, salinity, and steric height in the global ocean from the Argo Program, *Prog. Oceanogr.*, *82*(2), 81–100.
Scharroo, R., E. W. Leuliette, J. L. Lillibridge, D. Byrne, M. C. Naeije, and G. T. Mitchum (2012), RADS: Consistent multi-mission products, in *Proceedings of Symposium on 20 Years of Progress in Radar Altimetry*, vol. 20, ESA Communications, Noordwijk, Netherlands.
Strassburg, M. W., B. D. Hamlington, R. R. Leben, P. Manurung, J. Lumban Gaol, B. Nababan, S. Vignudelli and K. Y. Kim (2015), Sea level trends in Southeast Asian seas, *Clim. Past*, *11*(5), 743–750.
Tamisiea, M. E., E. M. Hill, R. M. Ponte, J. L. Davis, I. Velicogna, and N. T. Vinogradova (2010), Impact of self-attraction and loading on the annual cycle in sea level, *J. Geophys. Res.*, *115*, C07004, doi:10.1029/2009JC005687.
Tangdamrongsub, N., P. G. Ditmar, S. C. Steele-Dunne, B. C. Gunter, and E. H. Sutanudjaja (2016), Assessing total water storage and identifying flood events over Tonlé Sap basin in Cambodia using GRACE and MODIS satellite observations combined with hydrological models, *Remote Sens. Environ.*, *181*, 162–173.
Vinogradov, S. V., R. M. Ponte, P. Heimbach, and C. Wunsch (2008), The mean seasonal cycle in sea level estimated from a data-constrained general circulation model, *J. Geophys. Res.*, *113*, C03032, doi:10.1029/2007JC004496.
Von Schuckmann, K., J. B. Sallée, D. Chambers, P. Y. Le Traon, C. Cabanes, F. Gaillard, S. Speich, and M. Hamon (2014), Consistency of the current global ocean observing systems from an Argo perspective, *Ocean Sci.*, *10*(3), 923–949.
Wada, Y., L. P. H. Van Beek, and M. F. Bierkens (2011), Modelling global water stress of the recent past: On the relative importance of trends in water demand and climate variability, *Hydrol. Earth Syst. Sci.*, *15*(12), 3785–3808.
Wahr, J., M. Molenaar, and F. Bryan (1998), Time variability of the Earth's gravity field: Hydrological and oceanic effects and their possible detection using GRACE, *J. Geophys. Res.*, *103*(B12), 30,205–30,229.
Watkins, M. M., D. N. Wiese, D.-N. Yuan, C. Boening, and F. W. Landerer (2015), Improved methods for observing Earth's time variable mass distribution with GRACE using spherical cap mascons, *J. Geophys. Res. Solid Earth*, *120*, 2648–2671, doi:10.1002/2014JB011547.
Widlansky, M. J., A. Timmermann, S. McGregor, M. F. Stuecker, and W. Cai (2014), An interhemispheric tropical sea level seesaw due to El Niño Taimasa, *J. Clim.*, *27*(3), 1070–1081.
Wijffels, S., and G. Meyers (2004), An intersection of oceanic waveguides: Variability in the Indonesian through flow region, *J. Phys. Oceanogr.*, *34*(5), 1232–1253.
Willis, J. K., D. P. Chambers, and R. S. Nerem (2008), Assessing the globally averaged sea level budget on seasonal to interannual timescales, *J. Geophys. Res.*, *113*, C06015, doi:10.1029/2007JC004517.
Woodworth, P. L. (2011), A note on the nodal tide in sea level records, *J. Coastal Res.*, *28*(2), 316–323.
Zhang, X., and J. A. Church (2012), Sea level trends, interannual and decadal variability in the Pacific Ocean, *Geophys. Res. Lett.*, *39*, L21701, doi:10.1029/2012GL053240.
Zhang, S., M. J. Harrison, A. Rosati, and A. Wittenberg (2007), System design and evaluation of coupled ensemble data assimilation for global oceanic climate studies, *Mon. Weather Rev.*, *135*(10), 3541–3564.
Zheng, F., L. Feng, and J. Zhu (2015), An incursion of off-equatorial subsurface cold water and its role in triggering the "double dip" La Niña event of 2011, *Adv. Atmos. Sci.*, *32*(6), 731–742.
Zuo, H., M. A. Balmaseda, and K. Mogensen (2015), The new eddy-permitting ORAP5 ocean reanalysis: Description, evaluation and uncertainties in climate signals, *Clim. Dyn.*, 1–21.